Investigation and Enhancement of the Biocompatibility of CoCrAlSi Shape Memory Alloy

by

Ahmet Cemal Onat

A Dissertation Submitted to the
Graduate School of Sciences and Engineering
in Partial Fulfillment of the Requirements for
the Degree of

Master of Science
in
Mechanical Engineering

KOÇ ÜNİVERSİTESİ

September, 2025

Investigation and Enhancement of the Biocompatibility of CoCrAlSi Shape Memory Alloy

Koç University

Graduate School of Sciences and Engineering

This is to certify that I have examined this copy of a master's thesis by

Ahmet Cemal Onat

and have found that it is complete and satisfactory in all respects,
and that any and all revisions required by the final
examining committee have been made.

Committee Members:

_____

Prof. Demircan Canadinç

_____

Prof. Murat Sözer

_____

Assoc. Prof. S. Mine Toker

Date: _____

ABSTRACT

Investigation and Enhancement of the Biocompatibility of CoCrAlSi Shape Memory Alloy

Ahmet Cemal Onat

Master of Science in Mechanical Engineering

September 18, 2025

Current study investigates the biocompatibility of a novel CoCrAlSi shape memory alloy for orthopedic implant applications. The alloy was fabricated by vacuum induction melting and characterized using SEM, XRD, and XPS. A silver thin film, about 1000 nm thick, was deposited by physical vapor deposition to improve corrosion resistance. The silver coated samples were tested in phosphate-buffered saline (PBS) under body-like conditions. Ion release was measured with ICP-MS and compared to values reported in the literature. The Ag coating significantly reduced Co and Cr release, with decreases up to 84.6% and 51.6%, respectively, after 28 days of immersion. However, the absolute values of Co and Cr remained above safe biological thresholds. The silver layer itself showed an initial burst release that decreased over time, while surface analysis confirmed the formation of protective oxide films. These results suggest that Ag thin films can improve corrosion behavior and support the potential use of CoCrAlSi alloys in biomedical implants, but further optimization of coating thickness and ion release control is required.

ÖZETÇE

CoCrAlSi Şekil Hafızalı Alaşımın Biyouyumluluğunun Araştırılması ve İyileştirilmesi

Ahmet Cemal Onat

Makine Mühendisliği, Yüksek Lisans

18 Eylül 2025

Bu çalışma, yeni bir CoCrAlSi şekil hafızalı alaşımın ortopedik implant uygulamalarındaki biyouyumluluğunu incelemektedir. Alaşım, vakum indüksiyon ergitme yöntemiyle üretilmiş ve SEM, XRD ve XPS yöntemleriyle karakterize edilmiştir. Korozyon direncini artırmak amacıyla yaklaşık 1000 nm kalınlığında gümüş ince film, fiziksel buhar biriktirme yöntemiyle kaplanmıştır. Kaplanmış numuneler, vücut benzeri koşullarda fosfat tamponlu salin içinde test edilmiştir. İyon salımı ICP-MS yöntemiyle ölçülmüş ve literatürdeki değerlerle karşılaştırılmıştır. Ag kaplama, Co ve Cr salımını önemli ölçüde azaltmış; 28 günlük daldırma sonunda sırasıyla %84,6 ve %51,6 oranında düşüş sağlamıştır. Ancak Co ve Cr'un mutlak değerleri biyolojik olarak güvenli eşiklerin üzerinde kalmıştır. Gümüş tabaka ise başlangıçta yüksek iyon salımı göstermiş, fakat bu değer zamanla azalmıştır. Yüzey analizleri, koruyucu oksit tabakalarının oluşumunu doğrulamıştır. Sonuçlar, Ag ince filmlerin korozyon davranışını iyileştirdiğini ve CoCrAlSi alaşımlarının biyomedikal implantlarda kullanım potansiyelini desteklediğini göstermektedir. Bununla birlikte, kaplama kalınlığı ve iyon salımının daha iyi kontrolü için optimizasyon gerekmektedir.

TABLE OF CONTENTS

LIST OF TABLES

LIST OF FIGURES

Chapter 1: INTRODUCTION

1.1 Background on Biomaterials

Over the past 50 years, the field of biomaterials has grown into a multidisciplinary domain, originating from early innovations like British ophthalmologist Harold Ridley's intraocular lens and expanding into fields such as drug delivery, tissue engineering, and diagnostic devices. Modern biomaterials now focus on biological integration through surface modification, bioinspired design, and 3D architectures to enhance healing and interaction with living systems [1]. Modern biomaterials include metals, ceramics, polymers, and composites, each with distinct advantages. Metallic biomaterials are widely used in implants (e.g. bone plates, screws, dental and joint replacements) due to their superior mechanical properties [2]. Ceramic materials such as alumina and zirconia offer high biocompatibility and wear resistance, making them ideal for load-bearing joint prostheses. Polymers are used in orthopaedics for their versatility and biodegradability, with applications ranging from bone cements to resorbable fixation devices. Composite biomaterials combine the properties of ceramics and polymers to mimic the natural structure of bone, offering improved mechanical strength.

1.1.1 Metallic Biomaterials

Metals can bear high loads and resist fracture better than most polymers or ceramics, making them ideal for load-bearing orthopedic and dental applications [3]. However, to be successful as implants, metals must also be biocompatible – meaning they resist degradation and adverse body reactions over long periods. Key requirements include a high corrosion resistance to prevent metal ion release, good wear resistance, appropriate mechanical properties (avoiding stress shielding), and use of alloying elements with low toxicity [2, 4]. Achieving this balance is critical for long-term implant functionality and patient safety.

Several classes of metallic biomaterials have been developed for use in the human body. Traditional non-degradable (permanent) metals include stainless steels, titanium-based alloys, cobalt–chromium alloys, and nickel–titanium alloys. More recently, biodegradable

metallic implants such as magnesium-based alloys and iron-based alloys have been explored for temporary applications [5]. Each category has specific properties, advantages, and limitations, which are summarized below. Additionally, Table 1.1-1 provides overview of listed material groups.

1.1.1.1 Stainless steels

Stainless steels are widely used in medical implants and surgical tools because they combine affordability, strength, corrosion resistance, and easy cleaning. They are classified into several types—such as austenitic, martensitic, ferritic, precipitation-hardening, and duplex stainless steels—each with specific properties and medical uses. Among implant-grade options, commonly applied grades include 316L, 316LVM, nitrogen-strengthened steels, and standardized types defined by ASTM (F1314, F1586, F2229, F2581) [6].

Austenitic stainless steels, particularly AISI 316L, were among the first metals used for permanent implants. 316L combines strength, toughness, and ease of fabrication at relatively low cost. Chromium provides corrosion resistance, while nickel stabilizes the austenitic structure. The “L” indicates low carbon (<0.03%), which reduces carbide precipitation and enhances corrosion resistance [7]. A key drawback is its high Young’s modulus (~190–210 GPa), far above that of cortical bone (~5–30 GPa) [2] [8]. Another limitation is ion release if the passive film is damaged. Nickel may trigger hypersensitivity, while chromium at high levels is toxic. Nevertheless, 316L spontaneously forms a protective chromium oxide film in physiological conditions. Current research explores nitrogen alloying and nickel-reduced stainless steels to improve biocompatibility [7].

1.1.1.2 Titanium-Based Alloys

Titanium alloys are widely used in implants for their biocompatibility and relatively low elastic moduli compared to stainless steel [3]. Commercially pure titanium (CP-Ti) and Ti–6Al–4V (Grade 5) are common in hip stems, dental implants, and spinal devices [3]. Ti–6Al–4V combines high strength-to-weight ratio with an elastic modulus of ~110 GPa, about half that of 316L stainless steel or Co–Cr alloys, which reduces stress shielding [3]. Its corrosion resistance arises from a stable TiO_2 passive film that limits ion release and supports bone integration [9].

A drawback of Ti–6Al–4V is the potential toxicity of trace Al and V ions. This has motivated the development of β-titanium alloys free of these elements, such as Ti–Nb–Ta–Zr (TNTZ) and Ti–Nb-based systems. These alloys offer moduli of 50–70 GPa, closer to bone, and in some cases show superelastic behavior. Ti–29Nb–13Ta–4.6Zr, for example, demonstrates ~60 GPa modulus, excellent corrosion resistance, and good cytocompatibility. Such alloys are promising for reducing stress shielding and improving implant longevity [3].

1.1.1.3 Magnesium-Based Alloys

Magnesium-based alloys have emerged as leading candidates for biodegradable implants such as resorbable bone screws, plates, and cardiovascular stents. Mg is attractive because it is an essential element in the body and its density and elastic modulus (~41–45 GPa) are closer to bone than those of stainless steel or titanium [10]. Moreover, when an Mg implant corrodes, the degradation products (Mg^{2+} ions) can be naturally metabolized or excreted, and the implant gradually dissolves – eliminating the need for a second surgery to remove it. For example, Mg-alloy screws can provide temporary support during healing and then safely absorbed by body.

Despite these advantages, current magnesium alloys corrode too rapidly in physiological conditions. The high reactivity of Mg in salt solutions causes accelerated galvanic and pitting corrosion, leading to early loss of mechanical integrity. Rapid Mg corrosion also produces hydrogen gas as a side product that is a gas bubble formation around the implant can disrupt surrounding tissues and increase local pH which may cause inflammatory or cytotoxic effects [10]. Strategies to slow the corrosion include alloying (e.g. with rare earths, Zn, Ca) and applying protective coatings. While advanced Mg alloys (AZ31, WE43, etc.) show improved corrosion control, achieving a predictable degradation rate remains a challenge. Research continues into surface treatments and alloy design to ensure Mg-based implants degrade at a safe, steady rate while maintaining sufficient strength during the healing period [4].

1.1.1.4 NiTi Alloys (Nitinol)

Nickel–titanium (Nitinol, ~50:50 Ni:Ti) is the most widely used shape memory alloy in biomedical applications. Its appeal lies in reversible phase transformations that enable the shape memory effect and superelasticity. These properties allow devices to deform and then return to their original shape. For instance, stents can be crimped for delivery and expand to their preset form at body temperature. Orthodontic archwires and guidewires maintain nearly constant forces over large strains due to superelasticity. Mechanically, Nitinol recovers ~6–8% strain in the austenitic phase, far greater than conventional metals (≤0.2%). It also demonstrates excellent fatigue resistance, making it suitable for long-term implants such as cardiovascular stents. Corrosion resistance in body fluids is comparable to Ti alloys, as form TiO_2-rich passive films. However, the presence of Ni within the oxide layer remains a concern for biocompatibility [11].

The main drawback of NiTi is its high nickel content (~50 at. %). Nickel can leach from the surface in vivo, particularly if the passive film is compromised. Released Ni^{2+} ions may trigger allergic reactions and cytotoxic effects in sensitive patients. Studies show that bare Nitinol implants release measurable nickel over time, raising concerns about long-term biocompatibility. To address this, surface modifications such as thickened TiO_2 layers or protective coatings are applied to limit Ni release.

1.1.1.5 CoCr-Based Alloys

Cobalt–chromium alloys are another longstanding family of medical alloys due to their excellent mechanical properties and exceptional corrosion resistance in physiological environments. These alloys derive their corrosion resistance primarily from a passive oxide film enriched with chromium, which remains stable under various bodily fluid exposures. Especially in chloride-rich environments like saline or blood plasma, CoCr alloys exhibit superior pitting and crevice corrosion resistance compared to stainless steels. Variants such as Co–Cr–Mo are widely applied in orthopedic implants, including total hip and knee replacements, owing to their high strength and wear resistance. However, their relatively high elastic modulus compared to bone continues to pose challenges regarding stress shielding effects [12]. More critically, CoCr implants have faced biocompatibility challenges due to metal ion release and wear debris. Cobalt and chromium ions can provoke adverse tissue reactions: elevated Co/Cr levels have been associated with

inflammation, fibrosis, and even genotoxic effects in periprosthetic tissues. In metal-on-metal hip implants, Co and Cr wear particles have caused cases of local tissue necrosis and systemic symptoms (a phenomenon termed “metallosis”) in certain patients [7]. Because of these issues, the use of CoCr alloys in new implant designs has become more cautious, focusing on improvements to their microstructure and the use of coatings or surface treatments to minimize ion release.

Interestingly, a new generation of CoCr-based shape memory alloys has recently been developed to combine superelastic functionality with the strength of Co–Cr. An example is a Co–Cr–Al–Si alloy (a type of Heusler-phase SMA) reported [13]. This novel alloy can undergo reversible martensitic transformation like NiTi and exhibits a superelastic strain up to ~17%, far exceeding that of traditional metals. Moreover, its Young’s modulus (in certain crystallographic orientations) was found to be on the order of 10–30 GPa – approaching that of bone. Such low-modulus, highly elastic CoCr-based material could alleviate stress shielding while providing exceptional flexibility. However, Co–Cr–Al–Si SMA still contains ~60% cobalt and 30% chromium, so the chronic release of these ions remains a central concern. Initial corrosion tests in simulated body fluid showed CoCrAlSi has a lower corrosion current density (~0.03 μA/cm²) than conventional CoCrMo and Ti–6Al–4V, indicating a degree of passivity [14]. Yet under more aggressive conditions (anodic polarization), the alloy exhibited transpassive dissolution and released significant Co^{2+} and Cr^{3+} ions. This underscores that without protective measures, CoCr-based SMAs could pose similar biocompatibility risks as earlier CoCr implants. This study investigates surface coating for CoCrAlSi to act as diffusion barriers and improve its long-term biocompatibility. CoCr alloys clearly have desirable mechanical qualities, but controlling their interaction with the body environment is vital for their safe use.

Table 1.1-1: Overview of Metallic Biomaterials [10]

Materials	Advantages	Disadvantages
Stainless steel	High wear resistance, low cost, easily available, acceptable biocompatibility	Allergic reaction, much higher modulus than bone, lack of biodegradability
Co-based alloys	High wear and corrosion resistance, fatigue strength	Biologically toxic, much higher modulus than bone, expensive, lack of biodegradability
Ti-based alloys	High biocompatibility and corrosion resistance, fatigue strength, light weight, low Young's modulus	Poor tribological properties, lack of biodegradability
Fe-based alloys	Trace element, biodegradable, high radial strength, superior mechanical properties	Very slow corrosion process, excessively slow degradation rate, inadequate match of mechanical properties to those of a natural bone, magnetic nature
Zn-based alloys	Trace element, biodegradable, biocompatible, easy to cast and process, good machinability, moderate corrosion resistance	Low strength and plasticity
Mg-based alloys	Trace element, biodegradable, biocompatible, having mechanical properties similar to those of bone	Low corrosion resistance against living body circumstances, rapid loss of mechanical integrity, hydrogen evolution and alkalization during degradation

1.2 Corrosion in Metallic Biomaterials

When metal implants are placed in the human body, they are exposed to an electrolytic environment (blood, interstitial fluid) that can induce corrosion. Corrosion is the chemical or electrochemical degradation of the metal, producing metallic ions and other reaction products. It is a critical issue for biomaterials because a corroding implant can lead to several problems. First, the release of metal ions into surrounding tissues can trigger inflammation or toxicity – for example, excess Ni, Co, or Cr ions can disrupt cellular

metabolism or provoke immune reactions. Second, corrosion can alter the local chemical environment (e.g. lowering pH or generating metal oxides/hydroxides), which may impair tissue healing or even dissolve bone matrix (as in the case of peri-implant osteolysis) [7]. Third, the loss of metal from the implant surface (general thinning or formation of pits/cracks) can compromise the implant's mechanical integrity and fatigue life. Thus, high corrosion resistance is a fundamental requirement for permanent implants [3]. Even "mild" corrosion can produce symptoms ranging from localized pain and swelling to systemic effects if enough ions circulate in the bloodstream. Over the long term, corrosion byproducts have been linked to implant loosening and failure. For instance, particulate and ionic debris from corroded joint replacements can lead to chronic inflammation and bone resorption (osteolysis) around the implant, jeopardizing its fixation [7]. Therefore, understanding and mitigating corrosion processes in vivo is essential to implant design.

1.2.1 Importance of Corrosion Resistance in Implants

A key aspect of biocompatibility is the resistance of implants to corrosion. Stable, passive alloys are usually well tolerated, with tissues forming a thin fibrous capsule. Corrosion, however, causes both local and systemic effects. Locally, corrosion products can trigger inflammation, fibrosis, or tissue necrosis. Systemically, released ions may accumulate in organs such as lymph nodes, liver, or kidney. Elevated serum levels have been reported in patients with stainless steel or CoCr implants. Cobalt and chromium ions can induce oxidative stress and DNA damage, while nickel is a common allergen. Metal–protein complexes may also elicit immune or allergic reactions, including Type IV hypersensitivity. Severe cases lead to metallosis, marked by tissue necrosis and grey discoloration in failed metal-on-metal implants. To mitigate these risks, modern alloys are designed to self-passivate, and standards (ASTM, ISO) set corrosion limits in simulated body fluids [7].

Wear debris and released metal ions from implants present long-term health risks. Elevated cobalt and chromium levels are of particular concern. These ions can induce toxicity, promote tumor-like reactions, and in the case of chromium, generate reactive oxygen species that damage DNA. Chromium exposure has also been associated with cancer, ulcers, and neurological disorders [14].

1.2.2 Types of Corrosion

Metallic implants can undergo various forms of corrosion, depending on the material and the in vivo environment:

1.2.2.1 Uniform Corrosion

Uniform corrosion is a general attack over broad surface. Pure iron implants, for instance, may dissolve relatively uniformly in corrosive media. Uniform corrosion is easier to predict and sometimes acceptable in biodegradable implants (like Mg or Fe alloys) [10, 15]. However, most biomedical alloys form passive films that prevent uniform dissolution; thus other localized modes are more common.

1.2.2.2 Pitting Corrosion

Pitting Corrosion is a highly localized form of corrosion that leads to small pits or holes in the surface. Pitting is often initiated when chloride ions (abundant in body fluids) locally break down the passive oxide film on metals like stainless steel, CoCr, or NiTi. Once a pit forms, it can become an autocatalytic site where acidity and chloride concentration drive further metal dissolution. Even highly corrosion-resistant alloys like Ti–6Al–4V and CoCrMo have a critical pitting potential, above which their passive film degrades and pits nucleate [7]. Pitting is dangerous because it is not readily visible but can significantly weaken the implant or release ions from the deep pits.

1.2.2.3 Crevice Corrosion

Crevice corrosion occurs in narrow, shielded regions of implants where fluid flow is restricted, such as screw threads or modular junctions. Limited oxygen diffusion creates a differential aeration cell, with the crevice acting as the anode and surrounding surfaces as the cathode. This imbalance leads to local acidification and chloride accumulation, which promote breakdown of the passive oxide layer. Stainless steel and CoCr alloys are particularly vulnerable, and the resulting damage often progresses unnoticed until severe degradation occurs [7, 16].

1.2.2.4 Galvanic Corrosion

Galvanic corrosion occurs when two dissimilar metals are electrically connected in the body's electrolyte-rich environment (e.g., interstitial fluid or blood plasma). The metal with the lower electrode potential (the anode) corrodes preferentially, while the more noble

metal (the cathode) is protected. This is especially important in modular implants composed of different alloys—for example, combining titanium screws with stainless steel plates. The galvanic potential difference drives ion migration and promotes accelerated degradation of the less noble component. Design strategies such as electrical insulation between components or using metals with close corrosion potentials can reduce this risk [7, 16].

1.2.2.5 Stress Corrosion Cracking (SCC)

Stress corrosion cracking is a serious failure mode that involves the synergistic action of tensile stress (either residual or applied) and a corrosive environment. Even metals with good overall corrosion resistance can suffer from SCC under certain mechanical and electrochemical conditions. In biomedical settings, microstructural heterogeneities or manufacturing defects (e.g., machining marks or cold work zones) can act as stress concentrators, where crack initiation begins. Once initiated, the crack can propagate rapidly through the implant under continued physiological loading, potentially leading to sudden and catastrophic failure. Alloys like stainless steel and CoCrMo are susceptible under specific conditions [7, 16].

1.2.2.6 Fretting Corrosion

Fretting corrosion is caused by repeated micro-motion between two contacting surfaces in the presence of bodily fluids. This is common at modular implant junctions, such as head–neck tapers in hip prostheses. The passive protective oxide layers are mechanically disrupted by micromotion, exposing fresh metal surfaces to the corrosive environment. This repetitive damage-regeneration cycle accelerates both wear and corrosion, leading to increased metal ion release and debris formation. The generated particles can provoke inflammatory responses and contribute to implant loosening or failure [7, 16].

1.2.2.7 Tribocorrosion

Tribocorrosion is the combined action of wear and electrochemical corrosion, commonly seen in metal-on-metal joint replacements. During sliding or rolling, protective oxide films are removed, exposing fresh surfaces to rapid corrosion. Unlike fretting, it occurs under continuous motion rather than localized micromotion. The process accelerates material loss, surface damage, and release of metal ions and particles, which may trigger inflammation, necrosis, or metallosis [7, 16].

In summarize, metallic implants may experience different corrosion mechanisms depending on the alloy composition, design, and physiological environment. While uniform corrosion is relatively predictable, localized processes such as pitting, crevice, or galvanic corrosion are more dangerous due to their hidden progression. Stress and motion related forms such as stress corrosion cracking, fatigue corrosion, and fretting or tribocorrosion, further accelerating damage by combining mechanical and chemical effects. Figure 1.2-1 illustrates these corrosion types schematically, highlighting the different ways implant degradation can occur during the corrosion process.

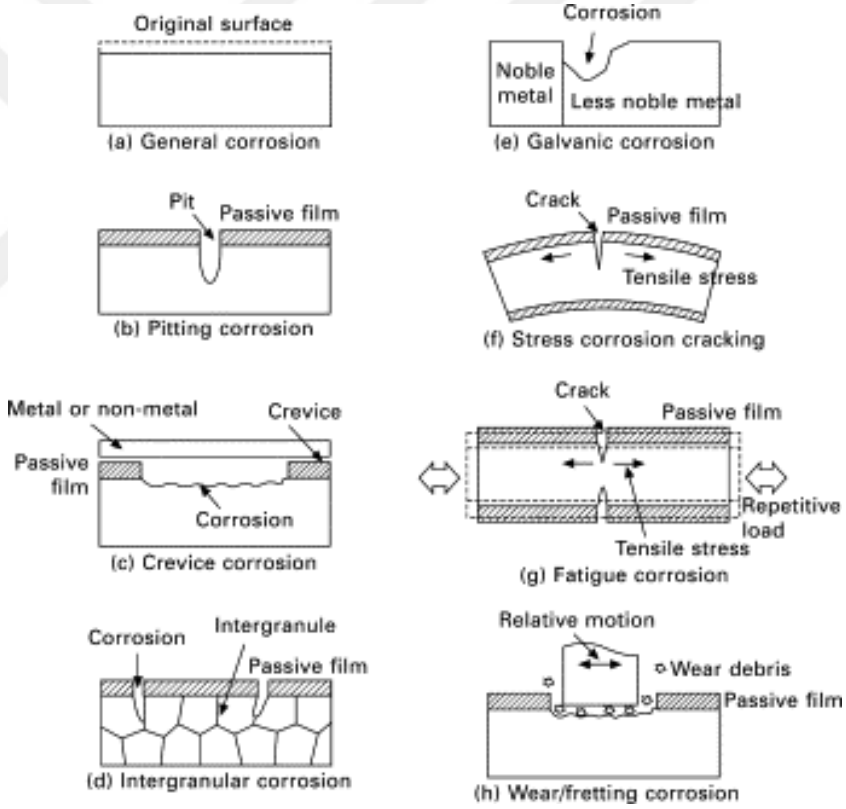

Figure 1.2-1 Types of Corrosion [17]

1.2.3 Surface Passivation and Oxide Films

Most metallic biomaterials rely on passive oxide films to resist corrosion in physiological environments. Passivation refers to the spontaneous formation of a thin, adherent oxide layer on the metal surface that dramatically slows down further oxidation. This passive film, typically a few nanometers thick, serves as a barrier that separates the bulk metal from the corrosive body fluids. Its protective role is fundamental to the biocompatibility and longevity of metallic implants [12].

The composition, thickness, and stability of these oxide films vary depending on the material and the biological environment. For instance, titanium and its alloys form a robust TiO_2 layer, known for its excellent corrosion resistance across a wide pH range, including inflammatory conditions [9, 12].

Importantly, the properties of the oxide film—its uniformity, defect density, and chemical composition—are highly influenced by both the alloy's microstructure and its surface treatment. For example, chemically passivated CoCr alloys exhibit significantly lower ion release in vitro compared to untreated samples, highlighting the benefits of controlled surface oxidation [18]. Similarly, multi-component alloys like Cr–Fe–Co–Ni–Mo systems have shown enhanced passivity and superior corrosion resistance due to synergistic interactions among alloying elements that stabilize the passive film [19].

However, despite their protective function, passive oxide layers are not immune to damage. Mechanical wear, scratching, or micromotions (fretting) at implant junctions can locally disrupt the film. If repassivation the rapid reformation of the oxide layer—does not occur swiftly enough, localized corrosion may initiate [20]. Moreover, aggressive species such as chloride ions in saline environments can penetrate or destabilize the passive layer, leading to pitting corrosion, especially in stainless steels and CoCr alloys [7].

1.3 Shape Memory Alloys

The discovery of shape memory alloys (SMAs) dates back to the early 20th century, when Arne Ölander reported unusual reversible deformation in Au–Cd alloys in 1932, followed by Greninger and Mooradian in Cu-based alloys in 1938 [21]. However, the phenomenon only gained broad recognition after William J. Buehler and Frederick Wang discovered the effect in equiatomic NiTi at the U.S. Naval Ordnance Laboratory in 1962, leading to the

development of Nitinol (nickel–titanium alloy), the most commercially important SMA [22]. This serendipitous finding opened pathways for wide-ranging applications in aerospace, engineering, and especially medicine.

SMAs are metallic materials characterized by their ability to recover a pre-defined shape through a solid-state, diffusionless phase transformation between a high-temperature austenite phase and a low-temperature martensite phase[23]. When cooled to martensite, they can be easily deformed, while heating above the transformation temperature restores the original form. Conversely, above the transformation temperature, applied stress can induce martensite that reverts upon unloading, producing superelasticity (or pseudoelasticity). These unique behaviors enable SMAs to exhibit large, reversible strains—up to several percent—far exceeding those of conventional metals [11]. Their combination of recoverable deformation, corrosion resistance, and biocompatibility makes them highly attractive for biomedical implants such as stents, bone staples, and orthodontic wires [23].

1.3.1 Shape Memory Effect

The shape memory effect (SME) refers to the ability of an alloy to “remember” and recover its original shape after being deformed in its martensitic phase and subsequently heated. Practically, an SMA is “programmed” into a shape in the austenitic state, then deformed while martensitic at low temperature. Upon reheating above the austenite finish temperature (A_f), the material undergoes a crystallographic transformation back to austenite, restoring the preset geometry [11]. This one-way SME is widely exploited in biomedical devices—for example, SMA bone plates that compress fractures when warmed, or self-deploying vascular stents activated by body temperature [23].

At the microstructural level, the SME arises from the reversible detwinning and reorientation of martensitic variants, rather than dislocation slip [21]. This crystallographic mechanism allows recovery of large strains (4–8% in NiTi) that would otherwise cause permanent plastic deformation in normal metals. Although repeated cycling may gradually shift transformation temperatures or reduce recovery, many SMAs can sustain thousands of cycles with minimal degradation [24]. Advanced alloying and processing strategies have further improved functional stability, enabling SMAs to serve as reliable actuators and

implant materials where controlled, repeatable shape recovery is critical [25]. Figure 1.3-1 shows the reversible transformation between austenite and martensite phases in shape memory alloys. Cooling transforms austenite into twinned martensite, which can deform under load, while subsequent heating restores the original austenitic structure.

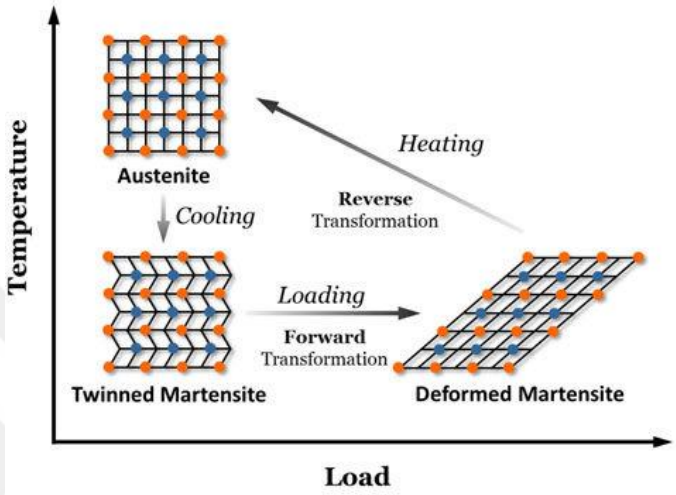

Figure 1.3-1 Principle of shape memory alloy (SMA) [26]

1.3.2 Shape Memory Alloys in Biomedical Applications

Shape memory alloys (SMAs) have attracted significant attention in biomedical engineering due to their unique properties such as the shape memory effect and pseudoelasticity, which enable them to recover pre-defined shapes under thermal or mechanical stimuli [27]. These characteristics allow SMAs to outperform conventional metallic biomaterials, especially in minimally invasive devices that require flexibility, adaptability, and long-term stability [28]. Their use spans across a wide range of applications including orthodontics, orthopedic fixation devices, cardiovascular stents, and scaffolds for regenerative medicine [27, 29]. Compared to traditional implant metals such as stainless steel or cobalt–chromium alloys, SMAs offer superior mechanical compatibility with biological tissues, better fatigue resistance, and the ability to exert nearly constant forces during functional loading.

Among SMAs, nickel–titanium (NiTi, or Nitinol) is by far the most extensively employed, particularly in dental and cardiovascular applications. In orthodontics, NiTi archwires apply light, continuous forces to achieve gradual tooth movement, while in vascular

interventions, self-expanding Nitinol stents adapt to vessel diameters and withstand cyclic loading without permanent deformation. NiTi has also been utilized in bone fixation plates, spinal rods, and minimally invasive surgical tools due to its combination of biocompatibility, corrosion resistance, and MRI compatibility [27, 29]. Beyond NiTi, however, other SMAs such as copper-based (Cu–Al–Ni) and iron-based (Fe–Mn–Si) alloys have been investigated. These alternatives demonstrate lower cost and tunable transition temperatures, although they typically suffer from inferior corrosion resistance and biocompatibility compared to NiTi [29].

Despite these advantages, the clinical adoption of SMAs is limited by several challenges. The most critical issue is biocompatibility, especially related to nickel ion release from NiTi devices, which can provoke cytotoxic or allergic reactions, necessitating protective coatings and surface treatments [28, 29]. Additionally, the mechanical mismatch between metallic SMAs and native tissues can lead to stress shielding in load-bearing implants, while fabrication challenges—such as processing high-melting-point alloys or achieving controlled porosity—further restrict broader use. Emerging approaches, including additive manufacturing of NiTi scaffolds and the development of Ni-free SMAs such as Co–Cr–Al–Si or Ti–Ta-based systems, seek to address these drawbacks by improving corrosion resistance, mechanical compatibility, and biological integration [28]. Overall, SMAs represent a promising class of smart biomaterials, with ongoing research focusing on optimizing their composition, processing, and surface modification to expand their safe and effective use in biomedical applications.

1.3.3 Mechanical Properties of SMAs

Shape memory effect (SME) and superelasticity (SE) behaviors enable SMAs to undergo large recoverable strains (up to 8–10% in tension for some alloys), high energy dissipation, and reversible phase transformations, making them mechanically unique compared to conventional metallic biomaterials. In addition to recoverable strain, properties such as elastic modulus, fatigue resistance, and fracture toughness determine their suitability for engineering and biomedical applications. Importantly, transformation temperatures, microstructural stability, and cyclic loading behavior strongly influence the long-term mechanical performance of different SMAs [23, 30].

Among the most studied alloys, NiTi (Nitinol) exhibits superior recoverable strain (~6–8%), excellent fatigue resistance under cyclic loading, and corrosion resistance comparable to Ti alloys. Its elastic modulus (30–83 GPa depending on processing and phase) is closer to that of bone than stainless steel or CoCr alloys, making it attractive for implants. However, its mechanical behavior is sensitive to composition and thermal treatments: Ni-rich NiTi tends to show lower transformation temperatures but increased hardness, while the presence of precipitates (e.g., Ni_4Ti_3) influences both transformation mechanisms and mechanical response [11, 23]. Cu-based SMAs (e.g., Cu–Zn–Al, Cu–Al–Ni) can reach recoverable strains above 15% and exhibit strong superelasticity, but their poor fatigue life and brittleness under thermal cycling limit long-term reliability. Similarly, Fe-based SMAs (e.g., Fe–Mn–Si) are low-cost alternatives with good strength and corrosion resistance, though they typically provide lower recoverable strains (<5%) and require external training to achieve stable SME [23, 30].

Recently, Co-based SMAs, especially Heusler-type alloys such as $Co_2Cr(AlSi)$ and off-stoichiometric compositions like $Co_{55}Cr_{25}Al_{10}Si_{10}$, have demonstrated promising mechanical performance. These alloys exhibit thermoelastic martensitic transformation with narrow hysteresis and superelastic recovery strains exceeding 2% in polycrystals [13]. Advanced single-crystal Co–Cr–Al–Si alloys further improved these properties, reaching recoverable strains up to 17% and a very low Young's modulus of 10–30 GPa—remarkably close to that of human bone—while maintaining high wear and corrosion resistance. Nevertheless, challenges such as grain boundary brittleness and elemental segregation remain, which can reduce toughness and lead to ion release in biomedical environments [14, 31]. To sum up, while NiTi remains the benchmark SMA for mechanical performance, ongoing research into Co- and Fe-based systems highlights their potential to combine low modulus, high recoverable strain, and biocompatibility, thereby expanding the mechanical design space for next-generation biomedical devices.

Table 1.3-1 summarizes the mechanical properties of various SMA systems, presenting their tensile yield strength (F_{yt}), compressive yield strength (F_{yc}), elastic modulus (E_A), and recoverable strain (ε_l). The data underline the superior strain recovery of NiTi and Cu-based

alloys and also indicating the growing potential of Fe- and Co-based SMAs for biomedical use.

Table 1.3-1 An overview of mechanical properties of SMAs for different compositions [30]

Alloys	Room temperature (°C)	F_{yt} (MPa)	F_{yc} (MPa)	E_A (GPa)	ε_l (%)
Ni-Ti	25	385	503	43	7.5
	25	336	469	26	7.5
	-	379	379	39.7	5.5
	-	401	401	62.5	6
	23–26	460.7	621.3	30.7	6
	-	435	-	68	8
	-	378	-	39.7	5.5
	-	401	-	62.5	6
	20–25	195-690	-	30	<8
	-	383	-	28	6
	-	414	-	27.5	6
Cu-Al-Mn	-	210	-	33.9	-
	20–25	160-180	-	20	12
	20–25	260	-	20	9
	-	210	-	28	9
Cu-Al-Be	23	235	-	32.04	5
Fe-Mn-Al-Ni	-	320	-	98.4	6.13
Fe-Mn-Si-Cr-Ni-1(V,C)	-	450	-	184	-
	23	310	-	200	1.15
	25.5	546	-	173	1.3
	25	546	-	173	-
	-	496-533	-	160	0.16–0.39
Fe-Ni-Co-Al-Ta-B	-	750	-	46.9	13.5

1.4 Surface Modification of Metallic Biomaterials

Surface modification is essential for improving the performance and biocompatibility of metallic biomaterials, especially in load-bearing implants. The main objective is to enhance corrosion and wear resistance without compromising the mechanical integrity of the substrate. Common techniques include physical vapor deposition (PVD), chemical vapor deposition (CVD), ion implantation, and thermal oxidation. Coatings such as diamond-like carbon (DLC), titanium nitride (TiN), and tantalum-based layers improve hardness, reduce friction, and minimize wear debris, thereby lowering the risk of aseptic loosening [32].

Engineered surfaces also support protein adsorption, cell adhesion, and osteointegration while reducing bacterial colonization and inflammatory responses [33]. Thin film methods such as magnetron sputtering further allow precise control of surface chemistry and morphology. Recent advances include high-entropy alloy (HEA) films doped with silver nanoparticles, which provide superior corrosion resistance, mechanical hardness, and antibacterial activity against Staphylococcus aureus and Pseudomonas aeruginosa, while maintaining cytocompatibility [34, 35].

1.4.1 Physical Vapor Deposition (PVD) Technique

Physical Vapor Deposition (PVD) is a widely used thin-film technique in which material from a solid source is vaporized and condensed onto a substrate under vacuum. The process involves vapor generation, transport, and condensation, and includes methods such as evaporation, sputtering, laser ablation, and arc deposition. Advanced approaches like reactive and magnetron sputtering enable precise control of film composition and structure [36]. PVD is especially valuable in biomedical applications as it modifies surface hardness, roughness, and chemistry without altering bulk properties, thereby improving wear resistance, corrosion resistance, and biocompatibility. It also allows deposition of multi-elemental and high-entropy alloy (HEA) coatings for novel biointerfaces [37].

Applications of PVD in metallic biomaterials demonstrate both mechanical and biological benefits. TiTaHfNbZr HEA coatings on Ti–6Al–4V and NiTi substrates produced dense films with superior wear resistance and reduced nickel ion release [38, 39]. Other HEA coatings suppressed Ni release in aggressive fluids and showed enhanced corrosion resistance and bioactivity through hydroxyapatite formation [40, 41]. Silver-modified HEA films have also been developed to provide antibacterial activity while maintaining mechanical stability [42]. These examples highlight PVD as a versatile surface modification method that improves implant durability and enables tailored functionalization for biomedical use.

1.4.2 Biomedical Coating Materials

Biomedical implant coatings can be classified according to their biological function and surface engineering properties. These coatings are designed to enhance the performance of metallic biomaterials—such as shape memory alloys or cobalt-chromium systems—by

improving corrosion resistance, enhancing biocompatibility, promoting osseointegration, and preventing bacterial infections. According to the comprehensive review by Faruq et al. [48], coating materials for implants are categorized into six main classes: Bioinert Ceramic Coatings, Bioactive Ceramic Coatings, Antibacterial Coatings, Polymeric Coatings, Carbon-Based Coatings, and Metallic Coatings. These categories reflect different surface modification strategies used for orthopedic and dental applications. A general comparison of their functional characteristics can be found in Table below.

Since the current study focuses on the improvement of biocompatibility and corrosion resistance of a novel CoCrAlSi shape memory alloy through silver-based coatings, only Metallic Coatings and Antibacterial Coatings will be discussed in detail in the following subsections.

1.4.2.1 Metallic Coatings

Metallic coatings are widely employed to enhance implant surfaces by improving corrosion resistance, biocompatibility, and mechanical compatibility. Titanium is the most common coating material, especially on less biocompatible substrates such as Co–Cr alloys. Plasma-sprayed Ti layers form stable TiO_2 passive films that reduce ion release and promote osseointegration through surface chemistry and roughness effects [43]. Other refractory metals, including tantalum and niobium, also improve implant performance. Their oxides (Ta_2O_5 and Nb_2O_5) are highly stable, chemically inert, and osteoconductive. For example, magnetron-sputtered Ta–O coatings on Ti–6Al–4V enhanced hardness, adhesion, and cell compatibility [44], while Nb_2O_5 coatings supported osteoblast adhesion and proliferation [45, 46]. These coatings are especially valuable for long-term implants in aggressive physiological conditions.

Emerging approaches extend metallic coatings to bioactive and multifunctional systems. Magnesium coatings deposited on porous Ti–6Al–4V scaffolds by arc ion plating provided a degradable interface that released osteogenic Mg^{2+} ions, stimulated bone regeneration, and improved osseointegration in vivo [47]. High-entropy alloy (HEA) coatings such as TiTaNbZrMo films have shown superior corrosion resistance, suppressed Ni release from NiTi substrates, and promoted hydroxyapatite formation [41]. Silver-based coatings deposited by plasma spraying on Co–Cr alloys yielded dense layers with antibacterial

activity and acceptable cytocompatibility [43]. Together, metallic coatings—ranging from Ti, Ta, and Nb to Mg, HEAs, and Ag-based systems—offer durable, corrosion-resistant, and biologically favorable surfaces, positioning them as integral solutions for next-generation orthopedic and dental implants [41, 43-47].

1.4.2.2 Antibacterial Coatings

Implant-associated infection is a serious complication in orthopedics, so antibacterial coatings have been developed to impart antimicrobial properties to implant surfaces. These coatings typically either release antimicrobial ions or drugs, or present a contact-killing surface to bacteria that attempt to colonize the device. Zinc oxide (ZnO), copper (Cu), silver (Ag), and biopolymer-based systems such as chitosan have all been investigated for this purpose. ZnO nanostructured coatings effectively generate reactive oxygen species and disrupt microbial membranes while maintaining high biocompatibility and low toxicity, making them cost-effective antibacterial agents, though their activity can depend on light activation and the use of composite systems for stable adhesion [48]. Copper-based coatings, including TiCuN and Ti–Cu oxides, inhibit bacterial biofilms and planktonic growth, but the release of Cu^{2+} ions must be carefully controlled because excessive levels are cytotoxic; optimized systems have achieved strong antibacterial activity while still supporting osteoblast function [49, 50].

Among metallic systems, silver coatings remain the most clinically validated due to their broad-spectrum antibacterial activity and relatively low cytotoxicity at controlled release levels. Silver ions (Ag^{+}) disrupt bacterial membranes and metabolic processes, providing long-term antimicrobial protection. Studies on Co–Cr alloys show that silver coatings deposited by plasma spraying create dense, uniform layers with strong antibacterial activity and no significant cytotoxicity [43]. Recent work also highlights that the antibacterial efficacy of Ag coatings can be tuned by deposition parameters, which control microstructure and ion release, balancing bacterial inhibition with host cell safety [42]. Furthermore, protective Ag layers significantly reduce cobalt and chromium ion release from Co–Cr alloys under variable saliva pH, directly improving implant biocompatibility [51]. These dual advantages—long-term antimicrobial defense and suppression of toxic metal ion release—were the rationale for selecting silver coatings in our work on Co–Cr–Al–Si shape memory alloys [43, 51].

In summary, metallic biomaterials are widely used in implant applications due to their strength and durability, yet their long-term success depends on controlling corrosion and minimizing toxic ion release. Shape memory alloys, especially NiTi and Co-based systems, provide unique properties such as superelasticity, shape recovery, and mechanical compatibility with bone, which make them attractive for biomedical use. However, their performance is strongly influenced by microstructural stability, corrosion resistance, and biocompatibility under physiological conditions. To address these challenges, surface modification techniques have been developed to improve passivation and to limit harmful metal ion release. Among these, physical vapor deposition allows the production of uniform thin films with controlled thickness and crystallinity, enabling enhanced corrosion protection and functional performance. In this context, silver coatings offer additional antibacterial properties while also serving as a protective barrier against substrate degradation. This thesis builds upon these concepts by investigating the corrosion behavior, ion release characteristics, and microstructural features of silver-coated CoCrAlSi alloys, with the aim of evaluating their potential as safe and effective implant materials.

Chapter 2: MATERIALS AND METHODS

2.1 Alloy Fabrication via Vacuum Induction Melting

The specimens were produced at the Institut für Werkstoffkunde, Germany, and were previously studied by H. C. Özdemir [14]. The Co55Cr25Al10Si10 (CCAS) alloy was fabricated by vacuum induction melting of high-purity elements in an Al_2O_3 crucible under argon using a VTC-200 Ti system. A three-stage melting process ensured homogeneity and phase control. The melt was first fully liquefied and degassed, then superheated under electromagnetic stirring to remove inclusions and achieve chemical uniformity. Finally, it was stabilized and cast into a copper mold. This process yielded defect-free ingots with a fine isotropic structure suitable for further processing [14].

The cast material was sectioned into coupons by electrical discharge machining (EDM) with dimensions of ~2 × 5 × 10 mm. Samples were then metallographically prepared and polished to mirror finish for characterization and corrosion testing.

2.2 Sample Preparation

2.2.1 Grinding & Polishing

All specimen faces were ground using a sequence of silicon carbide (SiC) abrasive papers of progressively finer grit sizes (800, 1000, 1200, 2000, and 2500 grit) utilizing polishing system located (Figure 2.2-2). This step removed machining marks and flattened the surfaces. After grinding, the samples were polished using a fine alumina slurry (0.3 μm Al_2O_3 particles) on a polishing cloth until a scratch-free, mirror-like finish was achieved, as shown in Figure 2.2-1. This meticulous polishing is critical to minimizing surface roughness and deformation, allowing accurate microstructural and surface chemical analyses. The final polished surface exhibited a clear reflectivity, indicating readiness for microscopy and spectroscopic characterization.

Figure 2.2-2 Polishing system

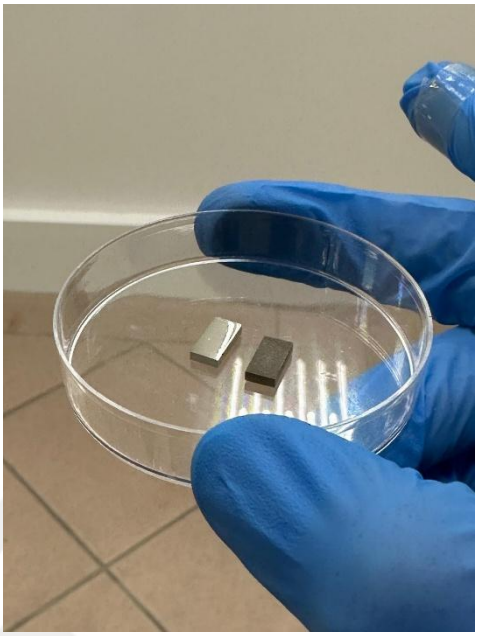

Figure 2.2-1 Polished sample surface

2.2.2 Ultrasonic Cleaning

Following polishing, the specimens were cleaned with ultrasonic cleaner (Figure 2.2-3) to remove any residual abrasive particles, oils, or contaminants from the surface. Each sample was immersed in organic solvents (e.g. acetone and ethanol) and subjected to ultrasonic agitation for ~10 minutes in each solvent bath. After cleaning, the samples were rinsed with distilled water and dried in air. This step ensured that the sample surfaces were chemically clean and free of impurities (like polishing alumina or grease) prior to coating or analytical procedures. Such solvent cleaning is a recommended practice to improve surface quality and reproducibility in corrosion tests.

Figure 2.2-3 Ultrasonic Cleaner

2.3 Characterization Techniques

Multiple analytical techniques were employed to characterize the alloy's phase composition, microstructure, and surface chemistry both before and after surface modification. The prepared CCAS specimens were analyzed by x-ray diffraction for phase identification, electron microscopy for microstructural observation and chemical analysis, and surface spectroscopy for elemental state analysis.

2.3.1 X-Ray Diffraction (XRD)

As shown in Figure 2.3-1, Bruker d2 phaser – x-ray diffractometer (XRD) was used to identify crystalline phases in the Co–Cr–Al–Si alloy and the Ag-coated samples. Bulk analysis was performed on a Bruker D2 Phaser diffractometer with Co Kα radiation (λ = 1.79 Å). Scans were collected in Bragg–Brentano geometry over 2θ = 30–120°, with a step size of 0.01° and 1 s per step. These conditions provided high-resolution patterns suitable for detecting ordered intermetallic phases. The peaks were compared with reference data to confirm the presence of $L2_1$ and $D0_{22}$ Heusler phases, which are linked to shape-memory behavior.

For the coated specimens, grazing-incidence XRD (GIXRD) was performed on a Bruker D8 Advance diffractometer, as shown in Figure 2.3-2. The X-ray beam was incident at ~1° to limit penetration to the film surface. Data were collected from 2θ = 30–100° with 1 s per step. This approach minimized substrate signals and revealed the coating structure. GIXRD confirmed the polycrystalline metallic Ag and allowed detection of any surface oxide phases.

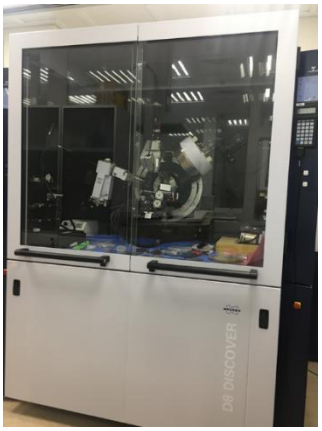

Figure 2.3-2 Bruker d8 discover x-ray diffraction system

Figure 2.3-1 Bruker d2 phaser – x-ray diffractometer

2.3.2 Scanning Electron Microscopy (SEM)

The polished alloy microstructure and coating morphology were examined using field-emission scanning electron microscopy. A Zeiss Ultra Plus FE-SEM (equivalent to Zeiss Supra series) was operated at accelerating voltages of 5–20 kV for high-resolution imaging, as shown in Figure 2.3-3. Uncoated CCAS samples revealed the grain structure and phase distribution of the alloy, while coated samples showed the surface topography of the deposited silver layer. The SEM images of the bare alloy (before coating) showed a polygonal grain structure with distinct regions along grain boundaries, later identified (via microanalysis) as Cr-rich segregations. After coating. SEM confirmed that the silver film was continuous and adhered well, with a densely packed, nanogranular morphology characteristic of sputtered Ag (visible as clusters of ~50–100 nm nodules).

Figure 2.3-3 Zeiss ultra plus field emission Scanning Electron Microscope (SEM)

2.3.2.1 X-Ray Photoelectron Spectroscopy (XPS)

XPS was employed to examine the surface chemistry and oxidation states of the alloy and silver-coated samples before and after immersion testing. Analyses were performed with a Thermo Scientific K-Alpha system, as shown in Figure 2.3-4, using a monochromatic Al Kα X-ray source (1486.6 eV). The instrument operated at 12 kV with a 400 × 400 µm spot size, and spectra were collected from areas a few hundred microns in diameter. Core levels

analyzed included Co 2p, Cr 2p, Al 2p, and Si 2p for the alloy, and Ag 3d, O 1s, and C 1s for the coated surfaces.

Binding energies were calibrated to the adventitious C 1s peak at 284.8 eV. High-resolution spectra were deconvoluted with Thermo Avantage software to identify chemical states. For the base alloy, XPS revealed the native oxide layer, including CoO and Cr_2O_3. For the Ag films, it confirmed elemental silver, checked for silver oxide, and identified possible contaminants. With a surface sensitivity of ~5 nm, XPS was critical for detecting oxide formation and monitoring changes at the coating–air and coating–solution interfaces.

Figure 2.3-4 Thermo K-Alpha X-Ray Photoelectron Spectrometer

2.4 Physical Vapor Deposition (PVD) Coating

Silver thin films were deposited by DC magnetron sputtering in a high-vacuum PVD chamber (Nanovak NVTS-400), as shown in Figure 2.4-1. Samples were cleaned (Section 5.2.2), dried, and mounted in the chamber. The base pressure was reduced to ~2.8 × 10^−6 Torr before introducing high-purity argon (99.99%). During deposition, the pressure was maintained at 1.85 × 10^−2 Torr with an argon flow rate of 10 sccm. A water-cooled silver target (99.99% Ag) was sputtered under 110 W DC power. Argon ions bombarded the target, releasing Ag atoms that condensed on the substrates.

Deposition was carried out at room temperature with a target–substrate distance of 15–20 cm for 40 minutes. Other operational parameters listed in Table 2.4-1. This produced a

uniform film of ~1 µm thickness, as estimated from calibration and verified experimentally. A silicon wafer was co-deposited and used to measure film thickness by cross-sectional SEM. The image revealed a dense, columnar structure with no large voids and a thickness of ~1.0–1.2 µm. The films adhered well to the 5 × 10 mm² samples and showed complete coverage. The process provided a pure Ag coating without high-temperature exposure, preserving the alloy's microstructure and shape-memory properties.

Table 2.4-1 PVD Coating Parameters

Experiment	DC Sputtering
Target	Silver (Ag)
Density	10.50 gr/cm³
z-ratio	0.529
Flow Rate	10 sccm
Duration of coating	40 min
Expected Thin Film Thickness	1000 nm
Chamber pressure beginning the sputtering	2.80×10^{-6} Torr
Chamber pressure during the sputtering	1.9×10^{-2} Torr

Figure 2.4-1 Nanovak Physical Vapor Deposition (PVD)

2.5 Biocompatibility Analysis

A series of immersion corrosion tests and analytical assays were conducted to evaluate the biocompatibility of the uncoated and Ag-coated alloy. The corrosion performance was assessed by exposing samples to a simulated physiological solution and measuring metal ion release, while surface analyses were performed to examine any compositional changes (such as oxide formation) on the material after immersion. The experimental design followed relevant ASTM standards for metal corrosion testing in vitro and aimed to simulate key aspects of the implant's service environment.

2.5.1 X-Ray Photoelectron Spectroscopy (XPS)

After immersion, XPS was performed to examine chemical changes on the silver-coated specimens. A Thermo K-Alpha system with an Al Kα source was used. Survey and high-resolution scans were collected for Ag 3d, O 1s, and base-metal signals where exposed. Samples had been immersed in phosphate-buffered saline. The aim was to identify oxidation states and possible corrosion products. Charge correction was applied to C 1s at 284.8 eV, and data were processed with the same peak-fitting method as for as-coated samples. New peaks or shifts indicated surface reactions. An increase in O 1s intensity or the presence of Ag–O in the Ag 3d spectrum suggested silver oxidation. Detection of P 2p or Na 1s peaks pointed to adsorption of buffer constituents. These results provided insight into the interaction between the Ag coating and the solution. They also indicated whether the film remained metallic or partially oxidized, which is critical for assessing corrosion resistance and long-term stability.

2.5.2 Static Immersion in Phosphate-Buffered Saline (PBS)

Static immersion corrosion tests were carried out in phosphate-buffered saline, a solution that simulates the ionic environment of body fluids. PBS (pH ≈ 7.4) was chosen as the immersion medium because of its stable and reproducible composition, making it standard for in vitro corrosion and ion release studies. Before immersion, each sample was partially masked so that only a well-defined surface area was exposed to the solution. Specifically, the specimens were embedded in a photopolymer resin leaving only the 5 mm × 10 mm face (the face coated with silver in coated samples) uncovered, as shown in Figure 2.5-1. To solidify photopolymeric resin Formlabs Form Cure L device used, as shown in Figure 2.5-2. The resin (a biocompatible epoxy or UV-cured polymer) was cured under UV light at

60 °C for 30 minutes to form a tight seal around the sample, thereby preventing crevice corrosion and restricting exposure to the intended surface. This preparation ensured that the surface area in contact with PBS was consistent (~0.5 cm² for each sample) and that immersion results could be normalized to area.

Each resin-sealed sample was immersed in an individual container with PBS. The solution volume followed ASTM G31, requiring ≥20 mL per cm² of exposed area. Accordingly, ~10 mL was used for ~0.5 cm² surfaces, preventing solution depletion or accumulation of corrosion products. Containers were kept at 37 ± 0.5 °C without agitation to mimic stagnant in vivo conditions. Test durations were 1, 7, 14, and 28 days. After each interval, both uncoated and Ag-coated samples were removed, rinsed with deionized water, dried, and the immersion solutions were collected for analysis.

Figure 2.5-1 Resin embedded samples

Figure 2.5-2 Formlabs Form Cure L

2.5.3 Inductively Coupled Plasma Mass Spectrometry (ICP-MS)

To quantify metal ions released from the samples during the PBS immersion tests, the collected solutions were analyzed using inductively coupled plasma mass spectrometry. ICP-MS is a highly sensitive technique capable of detecting trace metal concentrations at the parts-per-billion level, making it well-suited for evaluating biocorrosion of implants. An Agilent 7700x ICP-MS instrument, as shown in Figure 2.5-3, was employed to measure the concentration of Co, Cr, Al, Si (from the base alloy) and Ag (from the coating, if any dissolution occurred) in the immersion solutions. Before analysis, each PBS solution sample was acidified (with a small addition of high-purity nitric acid) to stabilize the ions and diluted to a volume appropriate for the ICP-MS calibration range. Standard solutions of the relevant metals were prepared to generate calibration curves for quantification.

The results from ICP-MS provided the cumulative release of metal ions (in μg/L) from each sample after the given immersion period. Comparing these values between uncoated and Ag-coated samples was critical to assess the effectiveness of the silver coating in suppressing ion leaching.

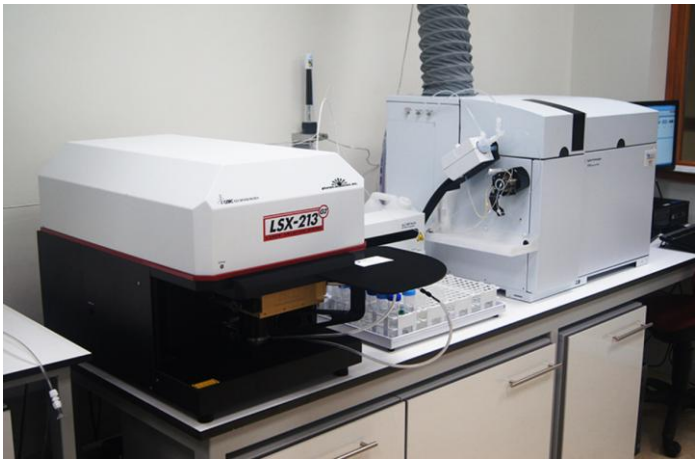

Figure 2.5-3 Agilent 7700x ICP-MS

Chapter 3: RESULTS

3.1 Microstructural Observations of CoCrAlSi

The SEM analysis of the CoCrAlSi alloy revealed a heterogeneous microstructure with elemental segregation along grain boundaries, where Cr and Si enrichment was accompanied by oxygen accumulation, while Co and Al were comparatively depleted [14]. Such segregation is consistent with observations in related Co-based Heusler systems, where phase separation and secondary precipitates were linked to brittleness and intergranular fracture [52]. As shown in Figure 3.1-1, the micrographs display a network of martensitic variants, while Figure 3.1-2 highlights the honeycomb-like structure at larger scale and visible grain boundaries at higher magnification. These features also indicated the coexistence of $L2_1$ and $D0_{22}$ phases, reflecting the martensitic transformation behavior reported for Co–Cr–Al–Si alloys [13, 14]. These microstructural features, particularly the presence of Cr- and Si-rich compounds at grain boundaries, are critical as they influence the passive oxide layer formation, corrosion resistance, and overall mechanical integrity of the alloy. In summary, the CoCrAlSi alloy exhibits a multiphase microstructure with significant boundary segregation, which is in line with findings on similar Co–Cr–Al–Si or Co–V–Al–Si systems, and these features play a decisive role in its performance as a potential biomedical implant material.

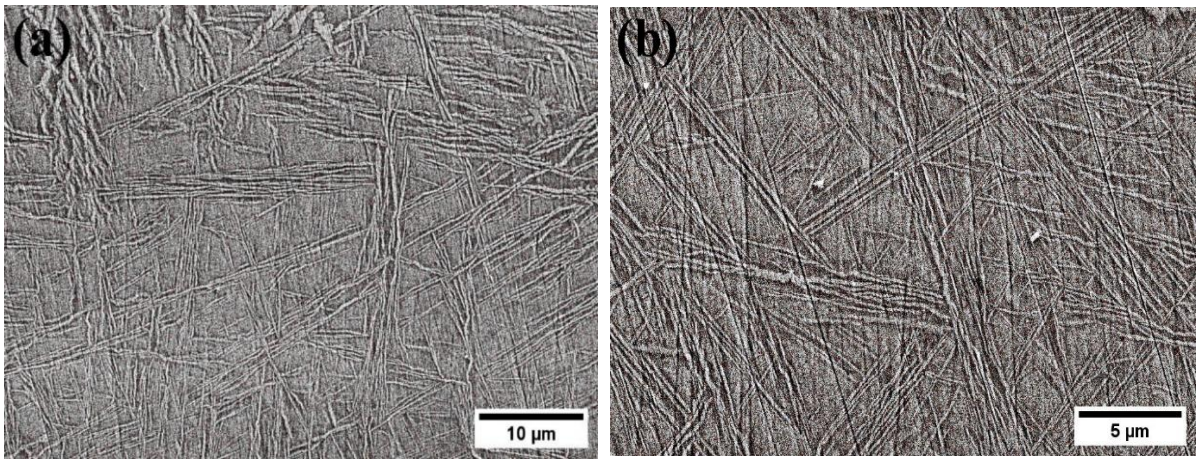

Figure 3.1-1 SEM Images of CoCrAlSi at scale of 10 µm (a) and 5 µm (b)

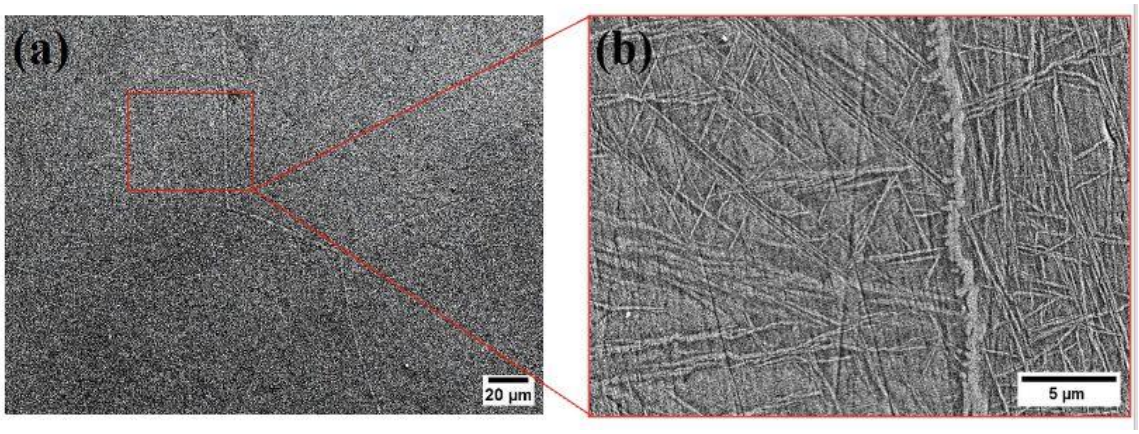

Figure 3.1-2 SEM Images of CoCrAlSi scale of (a) 20 µm visible honney-comb-like structure and (b) visible grain boundry at scale of 5 µm

3.2 Phase Identification and Crystallographic Analysis of CoCrAlSi (XRD)

Figure 3.2-1 shows the XRD pattern of bare alloy. The graph revealed the coexistence of both parent and martensitic phases, with the diffraction peaks corresponding primarily to the $L2_1$ austenite structure and the tetragonal $D0_{22}$ martensite structure, consistent with earlier studies on Co–Cr–Al–Si and related Heusler alloys [13, 14]. The presence of these phases indicates a thermoelastic martensitic transformation behavior, which has been widely reported for Co-based Heusler alloys [13, 52]. In addition to the main Heusler reflections, weak peaks associated with silicate compounds were also observed, suggesting elemental segregation and the formation of secondary phases, as noted in previous investigations of CoCrAlSi microstructures [14]. Similar to Co–V–(Si,Al) systems, where the martensitic transformation proceeds between $L2_1$ and $D0_{22}$ phases with high structural stability [53, 54], the CoCrAlSi alloy demonstrates a multiphase nature with retained parent $L2_1$ alongside martensite. Such crystallographic features are critical for understanding its functional properties, as the coexistence of ordered Heusler structures with secondary phases strongly influences both mechanical behavior and corrosion resistance.

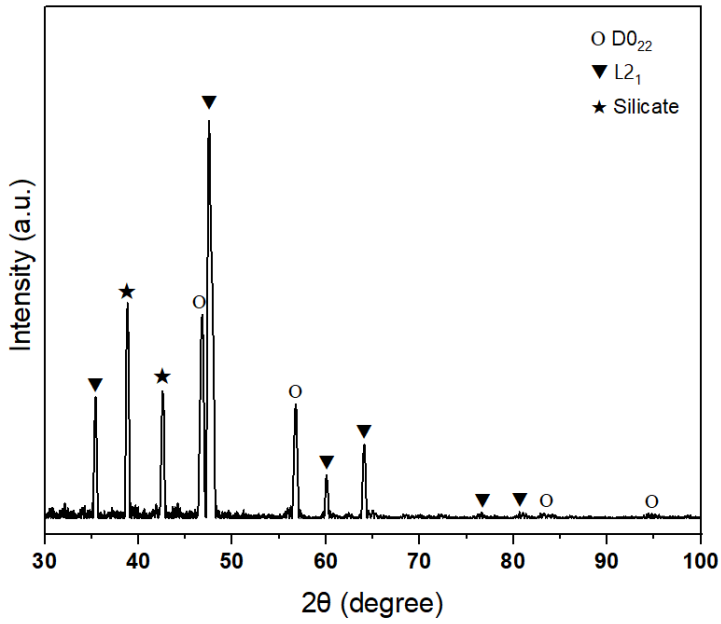

Figure 3.2-1 XRD pattern of CoCrAlSi

3.3 Surface and Cross Section Morphology of Thin film

The SEM images of silver coating, as shown in Figure 3.3-1, showed a continuous and compact thin film with dense grain packing, which is typical of sputtered silver layers. The surface morphology appeared smooth and homogeneous, without visible cracks or delamination, confirming that the PVD parameters were well controlled to achieve stable film growth. Such nanocrystalline and closely packed morphologies have been widely reported for sputtered silver thin films, where high surface energy promotes grain coalescence and uniform coverage [42]. The absence of voids or irregularities is consistent with the dense FCC (111) growth mode often observed in silver coatings, which contributes to mechanical stability and surface functionality.

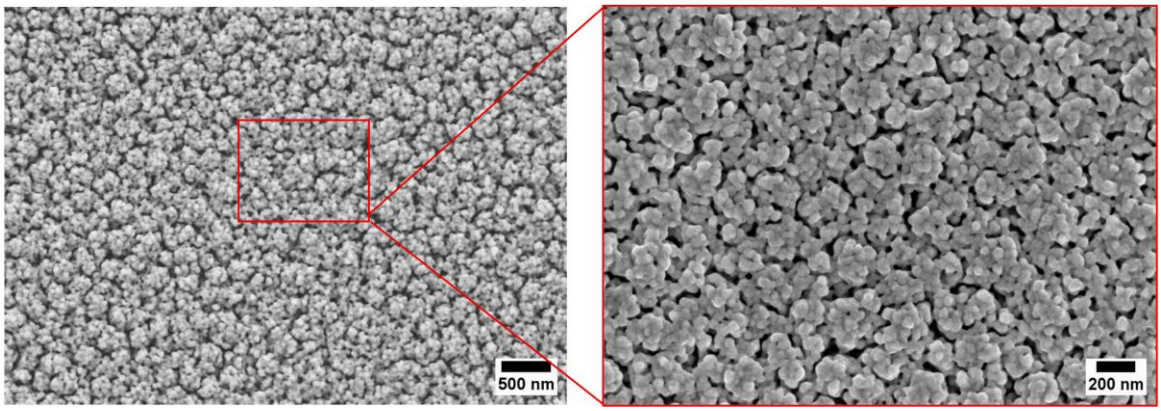

Figure 3.3-1 Surface Morphology of Silver Thin Film

The cross-sectional SEM images, as shown in Figure 3.3-2, confirmed that the thin film thickness was approximately 1000 nm, in line with the intended deposition design and expected outcome. The film exhibited a homogeneous columnar morphology across the section, with uniform thickness and strong adhesion to the substrate. This compact and well-structured growth is characteristic of magnetron sputtered silver layers, where deposition parameters control columnar development and crystallinity [42, 55]. The cross section revealed no delamination or significant porosity, indicating that the coating process produced a stable and continuous barrier. Such homogeneity and structural integrity are critical for ensuring the durability and performance of silver coatings in biomedical applications.

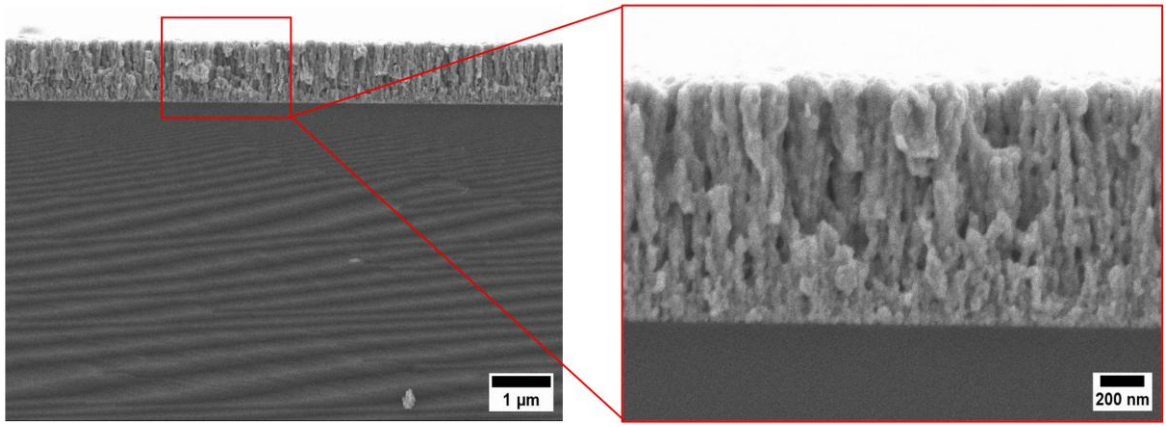

Figure 3.3-2 Cross section view of deposited silver thin film

3.4 Phase Identification of Thin Film (XRD, GI-XRD)

Figure 3.4-1 XRD pattern of silver thin film revealed characteristic peaks of face-centered cubic silver at 2θ ≈ 38.3° (111), 44.5° (200), and 64.7° (220), with the (111) reflection showing the highest intensity. This indicates a strong (111) preferred orientation, which is commonly observed in sputtered Ag coatings due to minimization of surface energy. In addition to Ag reflections, weaker peaks corresponding to oxides from the CoCrAlSi substrate, such as Cr_2O_3 and mixed $(Cr,Al)_2O_3$ phases, were also detected, along with minor signals from hcp-Co. These observations confirm that the deposited film is primarily composed of crystalline Ag with a pronounced (111) texture, while the substrate contributes secondary oxide-related reflections [42]. Table 3.4-1 and Table 3.4-2 provide information on the observed angle (2θ), relative intensity (a.u.), and the assigned phase/plane corresponding to each peak of XRD and GIXRD, respectively.

3.4.1 XRD (Ag Thin Film)

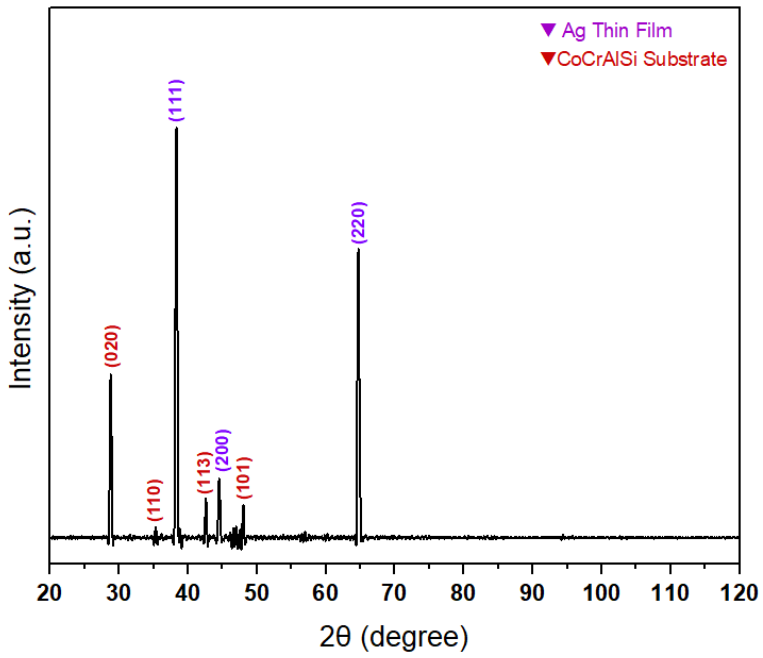

Figure 3.4-1 XRD pattern of silver thin film

Table 3.4-1 XRD peak table of silver thin film

Observed 2θ (°)	Rel. Intensity	Assignment (hkl or Phase)	Comments
28.8	~20	AlO(OH) Boehmite	The 28.8° peak matches boehmite (AlOOH) (020), formed by oxidation of Al in the CoCrAlSi layer.[56].
35.6	~5	Cr_2O_3 (110)	Secondary Cr_2O_3 peak from substrate [57].
38.3	100 (strongest)	Ag (111) (FCC silver)	The ~38.2° peak is fcc Ag (111) [59], showing dominant intensity and confirming strong (111) texture in the film.[58].
42.5	~10	(Cr,Al)_2O_3 (113)	The 42.6° peak fits a mixed $(Cr,Al)_2O_3$ corundum phase, lying between Cr_2O_3 (113) at 41.6° [60] and α-Al_2O_3 (113) at 43.3° [61], suggesting an oxide scale from the CoCrAlSi layer. [59] [60].
44.5	~15	Ag (200) (FCC silver)	The ~44.4° peak corresponds to fcc Ag (200), weaker than (111) and confirming preferred (111) orientation; overlap with hcp Co (002) at 44.5° is possible but minor.
48.0	~10	Co – HCP (101)	The ~48° peak likely comes from the CoCrAlSi layer, matching hcp Co (101). A $CoAl_2O_4$ spinel is less likely, as its stronger peaks near 31–37° are absent [61] [62].
64.7	~70	Ag (220) (fcc silver)	The ~64.6° peak corresponds to fcc Ag (220) [64], confirming crystalline Ag; overlap with Co_3O_4 (440) [65] or α-Cr_2O_3 (214) [66] is possible but less likely [63] [64] [65].

3.4.2 GI-XRD (Ag Thin Film)

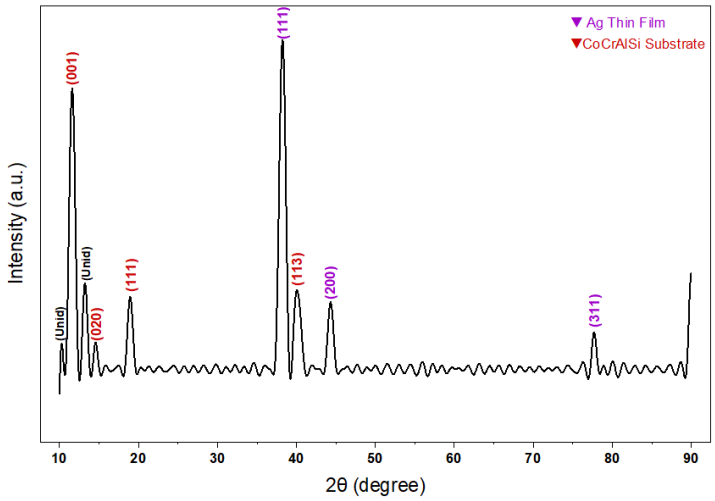

Figure 3.4-2 GIXRD pattern of silver thin film

Figure 3.4-2 GIXRD pattern of silver thin film displayed sharp peaks of fcc silver at 2θ ≈ 38.2° (111), 44.3° (200), and 77.7° (311). The strongest peak was (111), which indicates a clear preferred orientation in this direction. In addition to Ag peaks, weak reflections were present that arise from surface oxides of the CoCrAlSi substrate. Low-angle features suggest hydrated or layered phases, while signals near 14.5° and 18.9° match boehmite (γ-AlOOH) and cobalt spinel oxide (Co_3O_4). These results confirm that the film is mainly crystalline Ag with strong (111) texture, with minor oxide contributions from the substrate.

Table 3.4-2 GIXRD peak table of silver thin film

Observed 2θ (°)	Rel. Intensity	Assignment (hkl or Phase)	Comments
10.5	Low	unidentified	unidentified
11.6	High	Layered phase (e.g. Co–Al LDH or silicate)	d = 7.62 Å suggests a layered phase, likely Co–Al LDH or aluminosilicate, indicating a secondary surface layer [66] [67].
13.2	Moderate	unidentified	unidentified
14.5	Low	γ-AlOOH (boehmite) (020)	d = 6.06 Å matches boehmite (020) at ~14.5° [69], indicating a hydrated alumina layer formed by moisture-driven oxidation of Al [68].
18.9	Moderate	Co_3O_4 spinel oxide (111)	d = 4.68 Å matches the (111) reflection of Co_3O_4, suggesting an outer spinel layer formed on the CoCrAlSi substrate. Other spinel peaks may be weak or overlapped in grazing incidence geometry. [69].
38.2	High	Ag (111)	The fcc Ag (111) peak shows very high intensity, indicating strong (111) texture typical of sputtered Ag films [70] [71].
40.1	Moderate	Cr_2O_3	A minor peak near 40° is not from Ag and may originate from α-Cr_2O_3, which shows reflections at 38.5° and 41.2° [72].
44.3	Moderate	Ag (200)	The fcc Ag (200) peak is weaker than (111), confirming strong (111) texture, though some grains remain misoriented [73].
77.7	Low-Moderate	Ag (311)	The fcc Ag (311) peak [74] indicates minor random orientation, but the weak (220) and (222) confirm a strong (111) texture [73].

3.5 Chemical Composition and Oxide Formation (XPS)

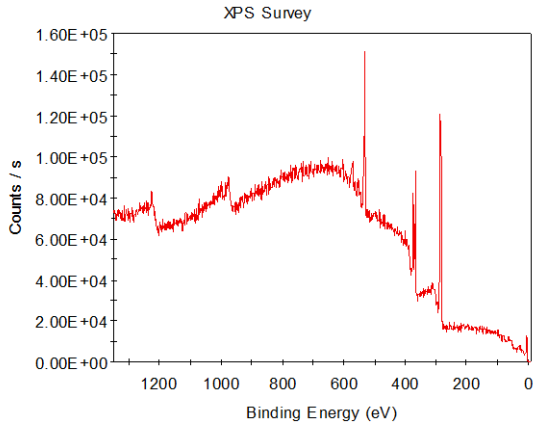

Figure 3.5-1 XPS survey of 1-day immersed Silver coated CoCrAlSi sample

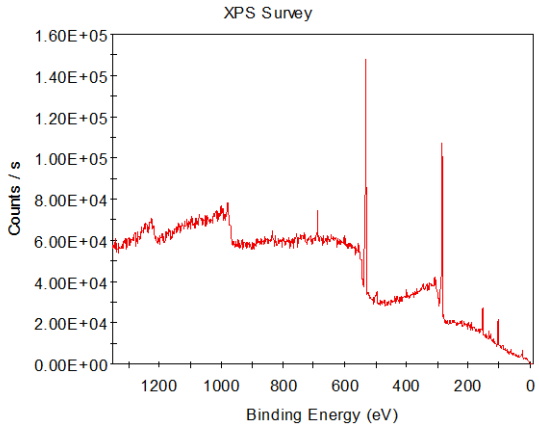

Figure 3.5-2 XPS survey of 28-days immersed Silver coated CoCrAlSi sample

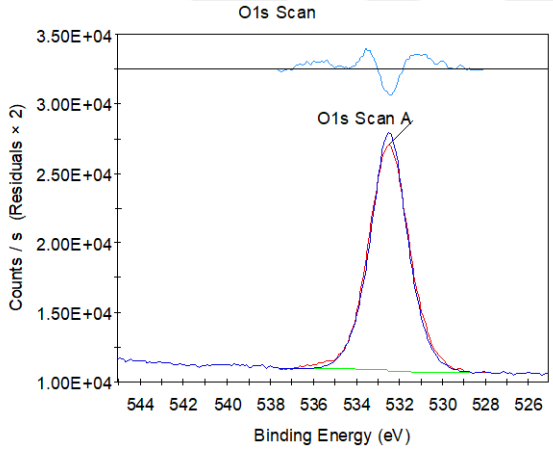

Figure 3.5-3 XPS graph of O1s scan of 1-day immersed Silver coated CoCrAlSi sample

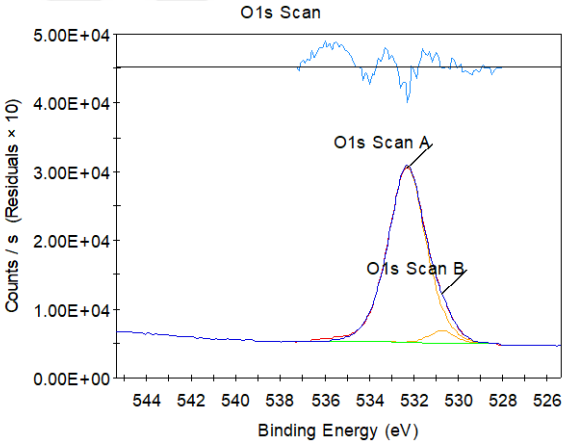

Figure 3.5-4 XPS graph of O1s scan of 28-days immersed Silver coated CoCrAlSi sample

Figure 3.5-1 and Figure 3.5-2 shows the XPS survey of the 1 day immersed silver coated alloy and 28 days immersed silver coated alloy, respectively. Also Figure 3.5-3 and Figure 3.5-4 shows XPS scan of O1s of 1 day immersed silver coated alloy and 28 days immersed silver coated alloy, respectively. The XPS analysis was conducted to evaluate the surface chemistry of the silver-coated CoCrAlSi samples after immersion in PBS. The survey spectra confirmed the presence of Ag together with O, Co, Cr, Al, and Si signals originating from the substrate and its oxides. After 1 day of immersion, the O 1s spectrum showed a single peak, indicating the formation of a simple oxide layer. After 28 days, the O 1s peak

deconvoluted into two components, suggesting the coexistence of metal oxides and hydroxides. This evolution indicates progressive oxidation and hydration of the surface, consistent with the tendency of CoCrAlSi to form mixed oxide films under immersion [42]. The results confirm that silver remained stable while the substrate contributed to oxide and hydroxide species over time.

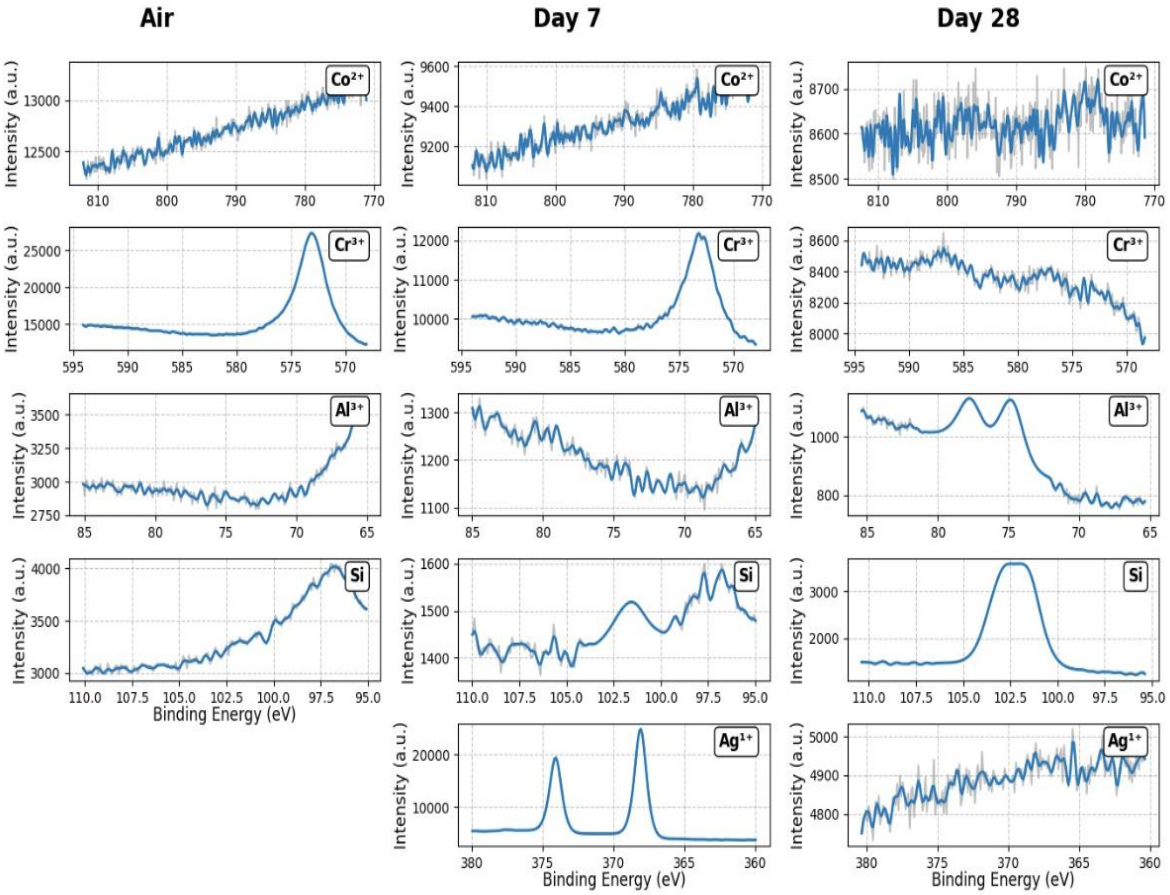

Figure 3.5-5 XPS spectra of Co-2p, Cr-2p, Al-2p, Si-2p, and Ag 3d (top down order) elements taken from the surface of silver coated CoCrAlSi specimen before (Air) and after immersed in PBS for 7 and 28 days.

Figure 3.5-5 shows the XPS spectra of each element over different immersed durations. Air inticates the non-coated CoCrAlSi alloy. XPS analysis was performed to investigate the surface chemistry of silver-coated CoCrAlSi before and after immersion in PBS. The survey spectra confirmed Ag together with Co, Cr, Al, and Si signals, reflecting contributions from both coating and substrate. The O 1s peak after 1 day appeared as a

single component, consistent with simple oxide formation, while after 28 days it split into two states, indicating oxides and hydroxides. High-resolution spectra showed that Co and Cr signals decreased with immersion, while Al and Si exhibited stronger oxide features, suggesting growth of a mixed oxide layer. In contrast, Ag peaks remained stable, confirming the persistence of metallic silver at the surface. These findings indicate progressive oxidation of the CoCrAlSi substrate with immersion time, while the Ag layer preserved its stability and surface presence [42].

3.6 Ion Release Behavior and Biocompatibility Implications

The ion release tests in PBS revealed distinct trends for Co, Cr, and Ag over 28 days. As shown in Figure 3.6-1, cobalt release decreased steadily from 17.3 ppb on day 1 to 8.9 ppb on day 28, indicating progressive stabilization of surface oxides. Chromium release fluctuated, showing an increase from 15.0 ppb on day 1 to 23.3 ppb on day 7, followed by a slight drop and then a rise to 25.3 ppb at day 28, suggesting unstable passive film formation. Silver release was initially low (7.0 ppb) but peaked at day 7 (82.3 ppb), then declined to 35.3 ppb at day 28, reflecting the dissolution and stabilization of the Ag coating. Compared with the uncoated CoCrAlSi substrate reported in SBF, which showed higher Co release throughout immersion, the silver-coated system effectively reduced cobalt dissolution. However, silver ions dominated the release profile, consistent with prior findings that sputtered Ag coatings exhibit strong (111) texture and controlled release behavior [14]. These results suggest that Ag coating mitigates Co-related cytotoxicity, while released silver provides antibacterial benefit, though its transiently high concentration highlights the importance of balancing antimicrobial activity with cytocompatibility.

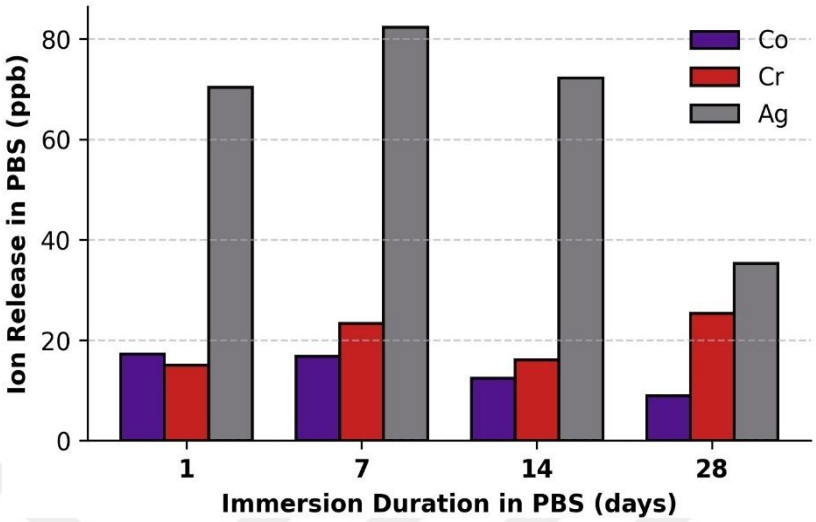

Figure 3.6-1 Ion release rate of silver coated CoCrAlSi sample for 1,7,14, and 28 days

3.7 Corrosion Morphology of Thin film

SEM images of corrosion of the 1-day immersed silver-coated CoCrAlSi specimen ,as shown in Figure 3.7-1, show the early onset of localized corrosion. At low magnification, the surface appears mostly uniform with few dark regions, while a distinct corrosion pit is visible in the center. High-magnification imaging highlights the pit morphology, with a smooth interior and roughened edges decorated by granular deposits. This indicates that corrosion initiated at a weak site or surface imperfection and progressed locally without widespread attack. The film largely remained intact after 1 day of immersion, consistent with early-stage pit formation that has also been reported for CoCr-based alloys exposed to simulated body fluids [14].

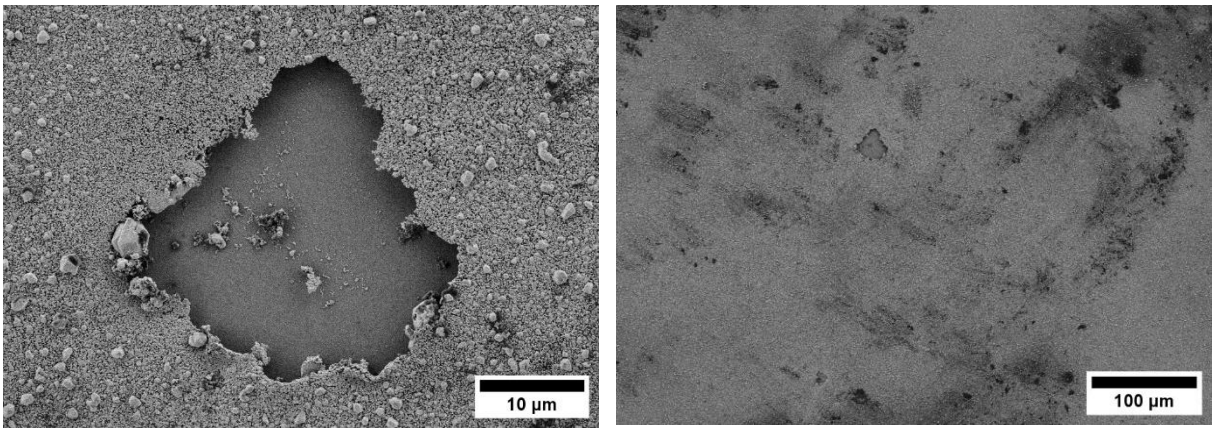

Figure 3.7-1 SEM images of the silver-coated CoCrAlSi sample after 1 day of immersion in PBS

The SEM observations of the thin film after 7 days of immersion in PBS, as shown in Figure 3.7-1, revealed distinct surface degradation features. The images show localized pitting and surface irregularities, which indicate breakdown of passive film and initiation of local corrosion. In particular, one region displayed a pronounced pit with a wide opening and irregular edges, reflecting advanced material loss and dissolution of underlying phases. The surrounding areas exhibited porous structures and fine-scale roughness, suggesting progressive attack along microstructural heterogeneities. The presence of both shallow porous regions and deep pits implies that corrosion was not uniformly distributed, but rather concentrated at sites associated with compositional segregation or defects. These findings are consistent with earlier reports on CoCr-based alloys, where elemental inhomogeneities at grain boundaries promote localized corrosion and ion release [7, 14]. The morphology after 7 days immersion confirms that the thin film is susceptible to localized degradation, with pits serving as preferential sites for continued dissolution and potential ion release.

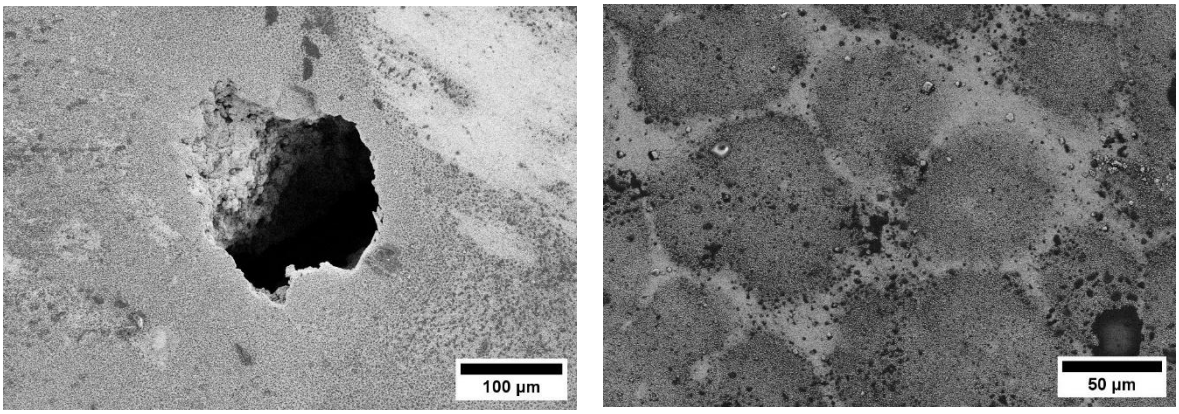

Figure 3.7-2 SEM images of the silver-coated CoCrAlSi sample after 7 days of immersion in PBS

3.8 Static Immersion Experiment Comparison with Previous Study

The static immersion experiments clearly highlight the improvement provided by the silver coating compared to the previous uncoated CoCrAlSi results. Comparison with the previous study has shown in both Figure 3.8-1 and Table 3.8-1 with the comparison table. In the coated samples, cobalt ion release decreased by more than 60% after one day and continued to drop, reaching an 84.6% reduction at day 28. Chromium ion release also showed lower values than the earlier study, though the reduction was less consistent across the immersion period. Meanwhile, silver ions were released into the medium, peaking at day 7 and gradually declining afterward. These results demonstrate that the silver coating effectively suppressed cobalt dissolution and partially reduced chromium release, while contributing its own ion release profile.

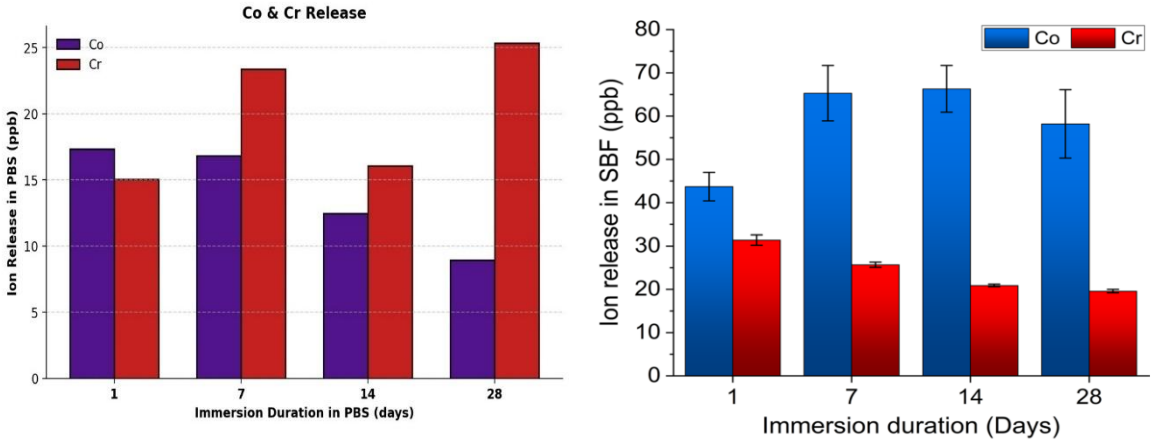

Figure 3.8-1 Co and Cr ion release comparison; current study (left), previous study (right)

Table 3.8-1 Ion release rate comparison table between current and previous study

	Day 1	Day 7	Day 14	Day 28
Co (ppm)	**17.3**	**16.8**	**12.5**	**8.9**
Co (ppm) (Previous)	**44**	**64**	**65**	**58**
Decrease in Co ion release (%)	**60.7%**	**75%**	**80.8%**	**84.6%**
Cr (ppm)	**15.0**	**23.3**	**16.0**	**25.3**
Cr (ppm) (Previous)	**31**	**25**	**22**	**21**
Decrease in Cr ion release (%)	**51.6%**	**8%**	**27.3%**	**17%**
Ag (ppm)	**70.4**	**82.3**	**72.3**	**35.3**

Chapter 4: DISCUSSION

4.1 Silver Coated CoCrAlSi Shape Memory Alloy as Biomedical Implant Material

Crystallite size in the PVD films increased with longer deposition times and higher argon flow rates. This trend reflects enhanced grain growth during prolonged sputtering and coarsening of crystallites under higher Ar flux. Similar behavior has been reported in FCC metallic films, where extended deposition promotes larger grains and strong Ag(111) texture. Argon flow also influenced nucleation density: low flow created many fine nanoparticles, while higher flow produced fewer and larger clusters. These microstructural changes are important since grain size and texture affect mechanical performance and ion release. In this study, a ~1000 nm coating thickness was selected as a practical optimum to form a continuous and stable layer. Literature supports this thickness: for example, diamond-like carbon films around 700–1000 nm on NiTi alloys improved both mechanical integrity and corrosion resistance [74]. A coating of ~1 μm provides sufficient adhesion and coverage without introducing excessive residual stress. Too thin coatings risk discontinuity, while overly thick coatings may suffer from stress accumulation. The chosen thickness therefore offered a balanced protection in the Co–Cr–Ag system.

Ion release data confirmed that the 1 μm Ag-containing coating significantly reduced Co and Cr leaching compared with the uncoated alloy. At all immersion times, Co and Cr concentrations were markedly lower than in the previous study [14]. Co release decreased by over 60% on day 1 and by about 85% by day 28. Cr release fell by more than 50% on day 1, though later reductions were smaller. For example, only 8.9 ppm Co was released at day 28, compared with 58 ppm in the uncoated case. Silver ions, in contrast, showed an initial burst release. Ag peaked at 70–80 ppm around day 7 and dropped to ~35 ppm by day 28. This pattern is typical for Ag-coated systems, where loosely bound surface silver dissolves quickly before stabilizing. Despite the reductions in Co and Cr, absolute levels remain a concern. Toxicity has been reported even below 19 ppb Co and 17 ppb Cr [75]. The ppm-range values observed here are orders of magnitude higher. Likewise, silver offers antibacterial benefits but can be toxic above ~1000–1500 ppb, while our early release levels were far higher. These results underline a trade-off. A thicker coating effectively blocks Co and Cr but increases the Ag reservoir and risk of toxic burst release. A thinner film reduces

Ag content but may not suppress substrate ion diffusion. Optimizing coating thickness and deposition conditions is therefore essential. The 1 μm Ag–Co–Cr coating improved corrosion resistance and lowered ion release overall, yet further refinement is needed to keep Ag within safe biological limits and maximize biocompatibility.

Chapter 5: CONCLUSIONS AND FUTURE WORK

1000 nm Ag coating significantly reduced Co and Cr ion release from the CoCrAlSi alloy compared to the uncoated material. Co release dropped by up to ~84.6% and Cr release by ~51.6% by day 28. This confirms a substantial improvement in corrosion resistance. However, the measured ion levels still remained above safe biological thresholds (~19 ppb for Co and ~17 ppb for Cr) reported as toxic The silver film showed an initial burst release of Ag ions (~70–80 ppm), which decreased to ~35 ppm by day 28. The coating also enhanced surface stability. It remained largely intact and promoted the formation of a protective oxide layer. These results suggest improved passivity and potential for better biocompatibility over time. Overall, the Ag–CoCr coated system shows strong promise for orthopedic implant applications due to its improved corrosion resistance.

Future work should focus on further optimization of the coating system. First, potentiodynamic polarization tests are needed to determine corrosion potential (E_corr) and corrosion current density (I_corr). These values will provide electrochemical performance data beyond static immersion results. Second, different coating thicknesses should be studied to identify a “sweet point” that balances silver release with suppression of Co and Cr leaching. Third, multilayer or graded coating designs may help reduce the initial burst of silver ions [76]. Finally, long-term immersion studies in protein-rich media are required. Such tests will better simulate physiological conditions, since proteins can strongly influence corrosion and ion release [77]. Together, these approaches can guide the development of safer and more effective Ag–CoCr coatings for biomedical implants.

BIBLIOGRAPHY

[1] B. D. Ratner and S. J. Bryant, "Biomaterials: where we have been and where we are going," *Annu Rev Biomed Eng,* vol. 6, pp. 41-75, 2004, doi: 10.1146/annurev.bioeng.6.040803.140027.

[2] B. H. B. Kuffner, P. Capellato, L. M. S. Ribeiro, D. Sachs, and G. Silva, "Production and Characterization of a 316L Stainless Steel/β-TCP Biocomposite Using the Functionally Graded Materials (FGMs) Technique for Dental and Orthopedic Applications," *Metals,* vol. 11, no. 12, 2021, doi: 10.3390/met11121923.

[3] M. Niinomi, Y. Liu, M. Nakai, H. Liu, and H. Li, "Biomedical titanium alloys with Young's moduli close to that of cortical bone," *Regen Biomater,* vol. 3, no. 3, pp. 173-85, Sep 2016, doi: 10.1093/rb/rbw016.

[4] K. K. Thomas, M. N. Zafar, W. G. Pitt, and G. A. Husseini, "Biodegradable Magnesium Alloys for Biomedical Implants: Properties, Challenges, and Surface Modifications with a Focus on Orthopedic Fixation Repair," *Applied Sciences,* vol. 14, no. 1, 2023, doi: 10.3390/app14010010.

[5] R. Davis *et al.*, "A comprehensive review on metallic implant biomaterials and their subtractive manufacturing," *Int J Adv Manuf Technol,* vol. 120, no. 3-4, pp. 1473-1530, 2022, doi: 10.1007/s00170-022-08770-8.

[6] "Medical Applications of Stainless Steels," in *Materials for Medical Devices*, vol. 23, R. J. Narayan Ed.: ASM International, 2012, p. 0.

[7] N. Eliaz, "Corrosion of Metallic Biomaterials: A Review," *Materials (Basel),* vol. 12, no. 3, Jan 28 2019, doi: 10.3390/ma12030407.

[8] Y. Li, C. Yang, H. Zhao, S. Qu, X. Li, and Y. Li, "New Developments of Ti-Based Alloys for Biomedical Applications," *Materials (Basel),* vol. 7, no. 3, pp. 1709-1800, Mar 4 2014, doi: 10.3390/ma7031709.

[9] M. Prestat and D. Thierry, "Corrosion of titanium under simulated inflammation conditions: clinical context and in vitro investigations," *Acta Biomater,* vol. 136, pp. 72-87, Dec 2021, doi: 10.1016/j.actbio.2021.10.002.

[10] S. Amukarimi and M. Mozafari, "Biodegradable magnesium-based biomaterials: An overview of challenges and opportunities," *MedComm (2020),* vol. 2, no. 2, pp. 123-144, Jun 2021, doi: 10.1002/mco2.59.

[11] A. Wadood, "Brief Overview on Nitinol as Biomaterial," *Advances in Materials Science and Engineering,* vol. 2016, pp. 1-9, 2016, doi: 10.1155/2016/4173138.

[12] B. G. Pound, "Corrosion behavior of metallic materials in biomedical applications. II. Stainless steels and Co-Cr alloys," *Corrosion Reviews,* vol. 32, no. 1-2, pp. 21-41, 2014, doi: 10.1515/corrrev-2014-0008.

[13] K. Hirata, X. Xu, T. Omori, M. Nagasako, and R. Kainuma, "Martensitic transformation and superelasticity in off-stoichiometric Co2Cr(AlSi) Heusler alloys," *Journal of Alloys and Compounds,* vol. 642, pp. 200-203, 2015, doi: 10.1016/j.jallcom.2015.03.264.

[14] H. C. Ozdemir, T. Blank, G. Gerstein, D. Canadinc, and H. J. Maier, "A preliminary assessment of the corrosion behavior of CoCrAlSi alloy as a

potential orthopedic implant material," *Journal of Materials Research,* vol. 40, no. 4, pp. 527-537, 2025, doi: 10.1557/s43578-024-01514-2.
[15] S. Virtanen, "Biodegradable Mg and Mg alloys: Corrosion and biocompatibility," *Materials Science and Engineering: B,* vol. 176, no. 20, pp. 1600-1608, 2011, doi: 10.1016/j.mseb.2011.05.028.
[16] "<[30] Biomedical Implants, Corrosion and its Prevention - A Review.pdf>."
[17] S. Hiromoto, "4 - Corrosion of metallic biomaterials," in *Metals for Biomedical Devices*, M. Niinomi Ed.: Woodhead Publishing, 2010, pp. 99-121.
[18] E. Moslehifard, T. Ghaffari, S. Mohammadian-Navid, M. Ghafari-Nia, A. Farmani, and F. Nasirpouri, "Effect of chemical passivation on corrosion behavior and ion release of a commercial chromium-cobalt alloy," *J Dent Res Dent Clin Dent Prospects,* vol. 14, no. 3, pp. 171-176, Summer 2020, doi: 10.34172/joddd.2020.037.
[19] X. Wang *et al.*, "Enhanced passivity of Cr-Fe-Co-Ni-Mo multi-component single-phase face-centred cubic alloys: design, production and corrosion behaviour," *Corrosion Science,* vol. 200, 2022, doi: 10.1016/j.corsci.2022.110233.
[20] M. Talha, Y. Ma, P. Kumar, Y. Lin, and A. Singh, "Role of protein adsorption in the bio corrosion of metallic implants - A review," *Colloids Surf B Biointerfaces,* vol. 176, pp. 494-506, Apr 1 2019, doi: 10.1016/j.colsurfb.2019.01.038.
[21] P. Nnamchi, A. Younes, and S. González, "A review on shape memory metallic alloys and their critical stress for twinning," *Intermetallics,* vol. 105, pp. 61-78, 2019, doi: 10.1016/j.intermet.2018.11.005.
[22] "<[32] The Story of Nitinol, The Serendipitous Discovery of the Memory Metal and Its Applications.pdf>."
[23] X. Yu *et al.*, "Mechanical behaviors and biomedical applications of shape memory materials: A review," *AIMS Materials Science,* vol. 5, no. 4, pp. 559-590, 2018, doi: 10.3934/matersci.2018.4.559.
[24] S. Samal *et al.*, "Recovery of deformation surface of superelastic and shape memory NiTi alloy," *Applied Surface Science Advances,* vol. 25, 2025, doi: 10.1016/j.apsadv.2024.100684.
[25] M. Chikhareva and R. Vaidyanathan, "A Thermal, Mechanical, and Materials Framework for a Shape Memory Alloy Heat Engine for Thermal Management," *Nanomaterials (Basel),* vol. 13, no. 15, Jul 25 2023, doi: 10.3390/nano13152159.
[26] W.-S. Chu *et al.*, "Review of Biomimetic Underwater Robots Using Smart Actuators (vol 13, pg 1281, 2012)," *International Journal of Precision Engineering and Manufacturing,* vol. 13, 07/01 2012, doi: 10.1007/s12541-012-0171-7.
[27] L. Petrini and F. Migliavacca, "Biomedical Applications of Shape Memory Alloys," *Journal of Metallurgy,* vol. 2011, pp. 1-15, 2011, doi: 10.1155/2011/501483.

[28] H. Wu *et al.*, "Current status and challenges of shape memory scaffolds in biomedical applications," *MedComm – Biomaterials and Applications,* vol. 3, no. 3, 2024, doi: 10.1002/mba2.95.
[29] "<[35] Shape memory alloys, Properties and biomedical applications.pdf>."
[30] A. Mohammadgholipour and A. M. Billah, "Mechanical properties and constitutive models of shape memory alloy for structural engineering: A review," *J Intell Mater Syst Struct,* vol. 34, no. 20, pp. 2335-2359, Dec 2023, doi: 10.1177/1045389X231185458.
[31] T. Odaira *et al.*, "Flexible and Tough Superelastic Co-Cr Alloys for Biomedical Applications," *Adv Mater,* vol. 34, no. 27, p. e2202305, Jul 2022, doi: 10.1002/adma.202202305.
[32] Z. A. Uwais, M. A. Hussein, M. A. Samad, and N. Al-Aqeeli, "Surface Modification of Metallic Biomaterials for Better Tribological Properties: A Review," *Arabian Journal for Science and Engineering,* vol. 42, no. 11, pp. 4493-4512, 2017, doi: 10.1007/s13369-017-2624-x.
[33] X. Hu, T. Wang, F. Li, and X. Mao, "Surface modifications of biomaterials in different applied fields," *RSC Adv,* vol. 13, no. 30, pp. 20495-20511, Jul 7 2023, doi: 10.1039/d3ra02248j.
[34] A. A. Alamdari *et al.*, "In vitro antibacterial and cytotoxicity assessment of magnetron sputtered Ti1.5ZrTa0.5Nb0.5W0.5 refractory high-entropy alloy doped with Ag nanoparticles," *Vacuum,* vol. 203, 2022, doi: 10.1016/j.vacuum.2022.111286.
[35] A. A. Alamdari, U. Unal, and A. Motallebzadeh, "Investigation of microstructure, mechanical properties, and biocorrosion behavior of Ti1.5ZrTa0.5Nb0.5W0.5 refractory high-entropy alloy film doped with Ag nanoparticles," *Surfaces and Interfaces,* vol. 28, 2022, doi: 10.1016/j.surfin.2021.101617.
[36] "<[47] Thin film deposition with physical vapor deposition and related technologies.pdf>," doi: 10.1116/1.1600450ㅅ.
[37] A. Mahajan and S. S. Sidhu, "Surface modification of metallic biomaterials for enhanced functionality: a review," *Materials Technology,* vol. 33, no. 2, pp. 93-105, 2017, doi: 10.1080/10667857.2017.1377971.
[38] N. Tüten, D. Canadinc, A. Motallebzadeh, and B. Bal, "Microstructure and tribological properties of TiTaHfNbZr high entropy alloy coatings deposited on Ti 6Al 4V substrates," *Intermetallics,* vol. 105, pp. 99-106, 2019, doi: 10.1016/j.intermet.2018.11.015.
[39] A. Motallebzadeh, M. B. Yagci, E. Bedir, C. B. Aksoy, and D. Canadinc, "Mechanical Properties of TiTaHfNbZr High-Entropy Alloy Coatings Deposited on NiTi Shape Memory Alloy Substrates," *Metallurgical and Materials Transactions A,* vol. 49, no. 6, pp. 1992-1997, 2018, doi: 10.1007/s11661-018-4605-4.
[40] C. B. Aksoy, D. Canadinc, and M. B. Yagci, "Assessment of Ni ion release from TiTaHfNbZr high entropy alloy coated NiTi shape memory substrates in artificial

saliva and gastric fluid," *Materials Chemistry and Physics,* vol. 236, 2019, doi: 10.1016/j.matchemphys.2019.121802.
[41] A. Hosseinjany, D. Canadinc, and M. B. Yagci, "Biocorrosion behavior TiTaNbZrMo high-entropy alloy thin films sputtered on NiTi shape memory alloy substrates with controlled microstructure," *Applied Surface Science,* vol. 661, 2024, doi: 10.1016/j.apsusc.2024.160038.
[42] H. C. Ozdemir, M. B. Yagci, E. Bedir, R. Yilmaz, and D. Canadinc, "Optimizing mechanical properties and Ag ion release rate of silver coatings deposited on Ti-based high entropy alloys," *Surface and Coatings Technology,* vol. 455, 2023, doi: 10.1016/j.surfcoat.2022.129221.
[43] R. Liang *et al.*, "Properties of silver contained coatings on CoCr alloys prepared by vacuum plasma spraying," *Mater Sci Eng C Mater Biol Appl,* vol. 106, p. 110156, Jan 2020, doi: 10.1016/j.msec.2019.110156.
[44] B. Rahmati *et al.*, "Development of tantalum oxide (Ta-O) thin film coating on biomedical Ti-6Al-4V alloy to enhance mechanical properties and biocompatibility," *Ceramics International,* vol. 42, no. 1, pp. 466-480, 2016, doi: 10.1016/j.ceramint.2015.08.133.
[45] M. S. Safavi, F. C. Walsh, L. Visai, and J. Khalil-Allafi, "Progress in Niobium Oxide-Containing Coatings for Biomedical Applications: A Critical Review," *ACS Omega,* vol. 7, no. 11, pp. 9088-9107, Mar 22 2022, doi: 10.1021/acsomega.2c00440.
[46] M. Fernandez-Lizarraga, J. Garcia-Lopez, S. E. Rodil, R. M. Ribas-Aparicio, and P. Silva-Bermudez, "Evaluation of the Biocompatibility and Osteogenic Properties of Metal Oxide Coatings Applied by Magnetron Sputtering as Potential Biofunctional Surface Modifications for Orthopedic Implants," *Materials (Basel),* vol. 15, no. 15, Jul 29 2022, doi: 10.3390/ma15155240.
[47] X. Li *et al.*, "Novel Bio-functional Magnesium Coating on Porous Ti6Al4V Orthopaedic Implants: In vitro and In vivo Study," *Sci Rep,* vol. 7, p. 40755, Jan 19 2017, doi: 10.1038/srep40755.
[48] V. Puspasari, A. Ridhova, A. Hermawan, M. I. Amal, and M. M. Khan, "ZnO-based antimicrobial coatings for biomedical applications," *Bioprocess Biosyst Eng,* vol. 45, no. 9, pp. 1421-1445, Sep 2022, doi: 10.1007/s00449-022-02733-9.
[49] C. Bergemann *et al.*, "Copper as an alternative antimicrobial coating for implants - An in vitro study," *World J Transplant,* vol. 7, no. 3, pp. 193-202, Jun 24 2017, doi: 10.5500/wjt.v7.i3.193.
[50] G. A. Norambuena *et al.*, "Antibacterial and Biocompatible Titanium-Copper Oxide Coating May Be a Potential Strategy to Reduce Periprosthetic Infection: An In Vitro Study," *Clin Orthop Relat Res,* vol. 475, no. 3, pp. 722-732, Mar 2017, doi: 10.1007/s11999-016-4713-7.
[51] R. Teixeira-Santos, M. Lima, L. C. Gomes, and F. J. Mergulhao, "Antimicrobial coatings based on chitosan to prevent implant-associated infections: A systematic review," *iScience,* vol. 24, no. 12, p. 103480, Dec 17 2021, doi: 10.1016/j.isci.2021.103480.

[52] "<[65] The Effect of Saliva pH and Protective Silver Coatings on Denture Base Materials (Cobalt Chromium Alloys) Ion Release.pdf>."
[53] K. Hirata, X. Xu, T. Omori, and R. Kainuma, "Phase stability and magnetic properties in Co2Cr(Al,Si) shape memory alloys," *Journal of Magnetism and Magnetic Materials,* vol. 500, 2020, doi: 10.1016/j.jmmm.2019.166311.
[54] K. Nakamura, A. Miyake, X. Xu, T. Omori, M. Tokunaga, and R. Kainuma, "Martensitic Transformation and Metamagnetic Transition in Co-V-(Si, Al) Heusler Alloys," *Metals,* vol. 11, no. 2, 2021, doi: 10.3390/met11020226.
[55] Y. Zhang, H. Jiang, X. Liu, L. Huang, S. Yang, and C. Wang, "Thermal cycle stability of Co64V15Si17Al4 high-temperature shape memory alloy," *Materials Letters,* vol. 260, 2020, doi: 10.1016/j.matlet.2019.126930.
[56] M. A. M. Khan *et al.*, "Structural and spectroscopic studies of thin film of silver nanoparticles," *Applied Surface Science,* vol. 257, no. 24, pp. 10607-10612, 2011, doi: 10.1016/j.apsusc.2011.07.058.
[57] X. Li *et al.*, "Aluminum (Oxy)Hydroxide Nanosticks Synthesized in Bicontinuous Reverse Microemulsion Have Potent Vaccine Adjuvant Activity," *ACS Appl Mater Interfaces,* vol. 9, no. 27, pp. 22893-22901, Jul 12 2017, doi: 10.1021/acsami.7b03965.
[58] K. Alshammari and A. H. Alshammari, "Synthesis of Cr2O3/C3N4 doped PVA polymer membranes for optoelectronic applications," *Polymer Testing,* vol. 141, 2024, doi: 10.1016/j.polymertesting.2024.108651.
[59] "<(111) Peak 3 Preparation of Silver Nanoparticle and Its Application to the Determination of ct-DNA.pdf>."
[60] "<(113) Peak 4 SYNTHESIS OF CHROMIUM OXIDE NANOPARTICLES AT DIFFERENT pH AND THEIR STRUCTURAL AND OPTICAL PROPERTIES.pdf>."
[61] F. R. Feret, D. Roy, and C. Boulanger, "Determination of alpha and beta alumina in ceramic alumina by X-ray diffraction," *Spectrochimica Acta Part B: Atomic Spectroscopy,* vol. 55, no. 7, pp. 1051-1061, 2000, doi: 10.1016/s0584-8547(00)00225-1.
[62] H. Xu, Q. Wu, M. Yue, C. Li, H. Li, and S. Palaka, "Effect of size distribution on magnetic properties in cobalt nanowires," *AIP Advances,* vol. 8, no. 5, 2018, doi: 10.1063/1.5006555.
[63] S. Taghavi Fardood, F. Moradnia, S. Ganjkhanlu, L. Ouni, A. Ramazani, and M. Sillanpää, "Green synthesis and characterization of spinel CoAl2O4 nanoparticles: Efficient photocatalytic degradation of organic dyes," *Inorganic Chemistry Communications,* vol. 167, 2024, doi: 10.1016/j.inoche.2024.112719.
[64] "<(220) Peak 7 Preparation of Silver Nanoparticle and Its Application to the Determination of ct-DNA.pdf>."
[65] C. Shin, J. Manuel, D. S. Kim, H. S. Ryu, H. J. Ahn, and J. H. Ahn, "Structural characterization and electrochemical properties of Co3O4 anode materials synthesized by a hydrothermal method," *Nanoscale Res Lett,* vol. 7, no. 1, p. 73, Jan 9 2012, doi: 10.1186/1556-276X-7-73.

[66] "<(220) Peak 7 SYNTHESIS OF CHROMIUM OXIDE NANOPARTICLES AT DIFFERENT pH AND THEIR STRUCTURAL AND OPTICAL PROPERTIES.pdf>."
[67] "<Peak 2 Thesis-2011-Papini.pdf>."
[68] A. T. M. Marsh, A. P. Brown, H. M. Freeman, B. Walkley, H. Pendlowski, and S. A. Bernal, "Determining aluminium co-ordination of kaolinitic clays before and after calcination with electron energy loss spectroscopy," *Applied Clay Science,* vol. 255, 2024, doi: 10.1016/j.clay.2024.107402.
[69] M. Y. Lee, F. S. Yen, and H. I. Hsiang, "Generating Self-Shaped 2D Aluminum Oxide Nanopowders," *Nanomaterials (Basel),* vol. 12, no. 17, Aug 26 2022, doi: 10.3390/nano12172955.
[70] Y. Liu, J. Xie, M. Luo, S. Jian, B. Peng, and L. Deng, "The synthesis and characterization of Al/Co 3 O 4 magnetic composite pigments with low infrared emissivity and low lightness," *Infrared Physics & Technology,* vol. 83, pp. 88-93, 2017, doi: 10.1016/j.infrared.2017.04.014.
[71] "<Peak 6 Synthesis of silver nanoparticles A safer alternative to conventional antimicrobial and antibacterial agents.pdf>."
[72] T.-H. Chuang, Y.-C. Lai, P.-I. Lee, and P.-C. Wu, "Characterization of (111)-Oriented Ag Nano-twinned Films on (111) Si Substrates," *International Journal of Mining, Materials, and Metallurgical Engineering,* 2021, doi: 10.11159/ijmmme.2021.002.
[73] P. Gibot, "Centimetric-Sized Chromium (III) Oxide Object Synthesized by Means of the Carbon Template Replication," *Ceramics,* vol. 3, no. 1, pp. 92-100, 2020, doi: 10.3390/ceramics3010010.
[74] "<Peak 8 Synthesis of silver nanoparticles, A safer alternative to conventional antimicrobial and antibacterial agents.pdf>."
[75] L. Geyao, D. Yang, C. Wanglin, and W. Chengyong, "Development and application of physical vapor deposited coatings for medical devices: A review," *Procedia CIRP,* vol. 89, pp. 250-262, 2020/01/01/ 2020, doi: https://doi.org/10.1016/j.procir.2020.05.149.
[76] S. Lischer *et al.*, "Antibacterial burst-release from minimal Ag-containing plasma polymer coatings," *J R Soc Interface,* vol. 8, no. 60, pp. 1019-30, Jul 6 2011, doi: 10.1098/rsif.2010.0596.
[77] O. Vasilev, A. Hayles, D. Campbell, R. Jaarsma, L. Johnson, and K. Vasilev, "Nanoscale antibacterial coatings incorporating silver nanoparticles derived by plasma techniques – A state-of-the-art perspective," *Materials Today Chemistry,* vol. 41, 2024, doi: 10.1016/j.mtchem.2024.102341.
[78] H. Zhang *et al.*, "Effects of serum proteins on corrosion rates and product bioabsorbability of biodegradable metals," *Regen Biomater,* vol. 11, p. rbad112, 2024, doi: 10.1093/rb/rbad112.